This is an EarthArXiV post-print of a manuscript accepted by *Geophys. J. Int.*

Outer Trench Slope Flexure and Faulting at Pacific Basin Subduction Zones

Emmanuel Soliman M. Garcia[1], David T. Sandwell[2], Dan Bassett[3]

[1] *Disaster Prevention Research Institute, Kyoto University, Gokasho, Uji, Kyoto 611-0011, Japan*

E-mail: garcia.soliman.2x@kyoto-u.jp

[2] *Scripps Institution of Oceanography, University of California, San Diego, La Jolla, CA 92093-0225*

[3] *GNS Science, 1 Fairway Drive, Lower Hutt, 5040, New Zealand*

SUMMARY

Flexure and fracturing of the seafloor on the outer trench wall of subduction zones reflects bending of the lithosphere beyond its elastic limit. To investigate these inelastic processes, we have developed a full non-linear inversion approach for estimating the bending moment, curvature, and outer trench wall fracturing using shipboard bathymetry and satellite altimetry derived gravity data as constraints. Bending moments and downward forces are imposed along curved trench axes and an iterative method is used to calculate the non-linear response for 26 sites in the circum-Pacific region having seafloor age ranging from 15 to 148 Ma. We use standard thermal and yield strength envelope models to develop the non-linear moment versus curvature relationship. Two coefficients of friction of 0.6 and 0.3 are considered and we find the lower value provides a better overall fit to the data. The main result is that the lithosphere is nearly moment saturated at the trench axis. The effective elastic thickness of the plate on the outer trench slope is at least three times smaller than the elastic thickness of the plate before bending at the outer rise, in agreement with previous studies. The average seafloor depth of the unbent plate in these 26

sites matches the Parsons & Sclater (1977) depth versus age model beyond 120 Ma. We also use the model to predict the offsets of normal faults on the outer trench walls and compare this with the horst and graben structures observed by multibeam surveys. The model with the lower coefficient of friction fits the fault offset data close to the trench axis. However, the model predicts significant fracturing of the lithosphere between 75 and 150 kilometres away from the trench axis where no fracturing is observed. To reconcile these observations, we impose a thermoelastic pre-stress in the lithosphere (Wessel 1992) prior to subduction. This pre-stress delays the onset of fracturing in better agreement with the data.

Key words: Numerical approximations and analysis; Lithospheric flexure; Mechanics, theory and modelling

1 INTRODUCTION

Subduction zones provide a natural laboratory for estimating the strength of the oceanic lithosphere. Walcott (1970) interpreted the topography of the outer rise observed seaward of Western Pacific trenches as an upward deflection caused by the bending of oceanic lithosphere as it subducts, and furthermore, suggested that this flexure can be modelled as the response to an applied force of a thin elastic plate floating on a fluid substratum. The flexural rigidity of the plate was identified as the key parameter that could predict the amplitude and wavelength of the concave-downward bending at the outer rise. For the Kuril Trench in particular, Hanks (1971) calculated that a horizontal force applied to a semi-infinite thin elastic plate having its origin at the trench axis could produce a flexural bulge similar to the outer rise, and predicted that the excess mass of the bent lithosphere there should then result in gravity anomalies which closely mimic the shape of the regional bathymetry. Indeed, an outer gravity high was observed in shipboard data collected at various subduction zones (Watts & Talwani 1974). The models discussed in Watts & Talwani (1974) expanded on the methods proposed in Hanks (1971) by also considering the effect of vertical shear forces, but it was Parsons & Molnar (1976) who developed an analytic framework which incorporated an applied bending moment at the trench. These various efforts eventually led to the formulation of a mathematical model for the flexure of a semi-infinite thin elastic plate resting on a fluid quarter-space and acted upon by the combination of a vertical force and a bending moment at one of its boundaries (Caldwell et al. 1976). This “universal elastic trench profile” was used to describe how the long-term regional deformation of a strong oceanic

lithosphere floating on an inviscid asthenosphere could generate the observed bathymetry and gravity features of the trench outer rise and slope.

Simple elastic flexure models provide a remarkably good fit to bathymetry and gravity data outboard of the trench axis (Caldwell et al. 1976). In addition, simple models of the cooling of the lithosphere give a reasonably accurate description of the increase in seafloor depth with age (Parsons & Sclater 1977). Assuming that the upper part of the lithosphere behaves elastically for temperatures less than $\sim 600^{\circ}$ C, the combination of the cooling and flexure models predicts that the elastic thickness, and thus flexural wavelength, of the lithosphere should depend on the age of the lithosphere. This elastic thickness versus age relationship has been adequately confirmed for moderate-sized seamounts (Watts 2001) but fails for flexure studies at subduction zones (Levitt & Sandwell 1995; Bry & White 2007) if a constant value for the elastic thickness is assumed to hold for the entire oceanic plate. However, when Hunter & Watts (2016) used an approach that incorporated variable elastic thickness by specifying an initial "seaward" value that would gradually decrease to a final "landward" value near the trench axis, they found that both sets of "seaward" and "landward" elastic thickness estimates trended upward with age. The decrease in elastic thickness as the plate approaches the trench axis could be considered as representing the inelastic deformation in lithosphere that is bent well beyond its elastic limit (Wessel 1992). The thin elastic plate flexure theory is accurate when the curvature of the flexed plate is small ($\sim 10^{-8} m^{-1}$). However, as the curvature is increased, the upper part of the plate yields by sliding on optimally oriented faults while the lower part of the plate yields by ductile flow processes (Goetze & Evans 1979; Mueller & Phillips 1995). At low curvatures there is an almost linear relationship between the bending moment and the curvature, so their ratio is equivalent to the flexural rigidity, which in turn is related to the cube of the elastic thickness. However, at high curvatures, the non-linear processes dominate and eventually the moment saturates. As the bending approaches moment saturation, the ratio of moment to curvature drops far below the initial elastic value and the elastic plate appears thinner (i.e. effective elastic thickness). McNutt & Menard (1982) developed a method for correcting the effective elastic thickness back to the true mechanical thickness using the measurements of maximum plate curvature combined with a model for the yield strength versus depth. While this approach can be accurate for plates bent at moderate curvatures ($\sim 10^{-7} m^{-1}$), it provides inaccurate results for plates bent at higher curvatures (Mueller & Phillips 1995). Moreover, bathymetric fractures on the outer trench walls of subduction zones may result in inaccurate estimates of curvature depending on the filtering technique applied (Craig et al. 2014a; Craig & Copley 2014). The combined effect is that converting effective elastic thickness to mechanical thickness may be in error by a factor of two or more (Levitt & Sandwell 1995), and it may explain why in that study, elastic thickness estimates from flexure models of trenches showed little or no increase with age.

Of course the lithosphere is bent well beyond its elastic limit at all subduction zones since the subducted part of the plate is permanently deflected away from the horizontal as it founders in the mantle. In this study we will focus on the end-member case where the lithosphere is approaching moment saturation at the trench axis. As shown in Mueller & Phillips (1995), the saturation bending moment increases almost linearly with increasing seafloor age for the half-space cooling model and shows some flattening at ages greater than about 70 Ma for the plate cooling model (Levitt & Sandwell 1995). Therefore accurate estimates of bending moment at the deepest part of each trench can be used to calibrate the temperature-dependent yield strength envelope models.

Rather than measure the characteristic wavelength and curvature of the flexure, we propose that the bending moment is the important parameter. Here we perform a circum-Pacific analysis of bathymetry and gravity outboard of trenches having a variety of seafloor ages to estimate the saturation moment as well as the depth and offset of the outer trench wall fractures. We use a thin-plate flexure model that can simulate trenches having curved planform (Garcia et al. 2015). In addition the model has a full non-linear relationship between moment and curvature according to a prescribed yield strength envelope (YSE, e.g., Goetze & Evans 1979). The new aspect of this analysis is that an iterative approach is employed to fit the non-uniform distribution of bathymetry and gravity data. The model has spatially variable applied bending moments and downward forces along the curved trench axis (Fig. 1). The starting model has an age-dependent flexural rigidity and a set of moment and load parameters is estimated. The curvature of the flexed plate is used to refine the spatially-variable rigidity and the least absolute deviations problem is re-solved until convergence is reached. The final model provides estimates of the moment at the trench axis, the depth of the fracturing in the upper part of the plate, and the overall strain in the uppermost part of the plate that can be related to the surface faulting. The main questions we will consider in this study are:

- Are the flexed plates at subduction zones close to moment saturation?
- Is an age-dependent YSE model consistent with the observations?
- Which combination of brittle, ductile, and thermal models is most consistent with the observations?

Our analysis is similar to the global compilation by Levitt & Sandwell (1995) and later work by Bry & White (2007) but with a few significant differences, foremost of which is that those studies used constant-rigidity thin plate flexure to model gravity and topography profiles. Meanwhile, recent efforts that attempted to improve upon them by developing methods for variable-rigidity plates instead (Hunter & Watts 2016; Zhang et al. 2017) are more closely related to our study, however, we will also mention some important distinctions in the details further below. The Levitt & Sandwell (1995) study limited the bathymetry to actual soundings while the Bry & White (2007) used actual soundings

averaged over segments outboard of the trench. Here we use a refined gravity model (Sandwell et al. 2014) and actual ship soundings that were recently updated (Olson et al. 2014). Moreover, rather than using only profiles that are nearly perpendicular to the trench, which greatly limit the areas to be modelled (Levitt & Sandwell 1995), we developed a flexural surface model defined over two horizontal dimensions to account for the actual 2-D geometry of the trench in map view. Therefore, all ship soundings in the area can be used to provide adequate coverage of locations both adjacent to and away from the trench. This can have an important effect where the planform of the trench is sharply curved (Manriquez et al. 2014). Any differences in geometry may be a concern not just for how data are included in an inverse modelling approach but also with regard to the results of the parameter estimation process. It was demonstrated in Wessel (1996) that using 1-D trench-perpendicular profiles instead of a 2-D plate to estimate elastic thickness using flexure models can result in values that are as much as 30 percent higher than the synthetic model thickness, when the applied bending moments and vertical loads are specified to vary along the trench axis. Most importantly, our model uses a full non-linear relationship between bending moment and curvature for a given YSE. This is in contrast to some previous approaches in which the variable elastic thickness of a plate is represented with discontinuous regions of constant thickness, or a "stair-step" form. Such stair-step variations in elastic thickness have been applied to modelling of trench-perpendicular profiles of bathymetry along the Chile (Contreras-Reyes & Osses 2010) and Mariana (Zhang et al. 2014) subduction zones, as well as for a selection of subduction zones globally (Zhang et al. 2017). In another study comparing the strength of the incoming plate across multiple trenches, ensemble average profiles of marine gravity anomalies within regions of and across entire circum-Pacific subduction zones were used as inputs for inverse modelling to obtain models of ramp-like variations of elastic thickness (Hunter & Watts 2016). The modelling of elastic thickness with a stair-step form has also been applied to plate regions outboard of the Chile trench (Manriquez et al. 2014), while arbitrary functional forms of the variation in elastic thickness were used for the incoming plate at the Manila trench (Zhang et al. 2018). Another approach that can result in continuous variations of elastic thickness is to implement a full elasto-plastic numerical simulation, but this has only been attempted for profiles at the Mariana subduction zone thus far (Zhou et al. 2015; Zhou & Lin 2018). Our methods are distinct from these prior efforts by allowing for a smooth and continuous variation in plate rigidity which is derived from a moment-curvature relation.

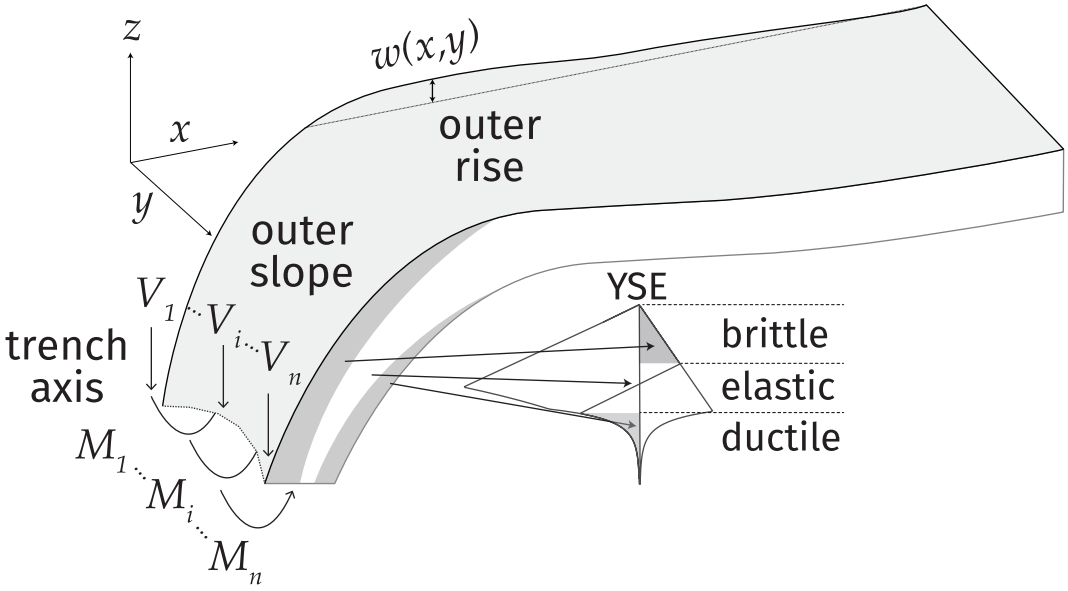

Figure 1. Thin elastic plate bent downward by moments and vertical loads acting along curved segments ($\sim$ 50 km long). The strength of each segment is adjusted so the model topography and gravity outboard of the trench match observations. The planform of the trench is digitised from (Bassett & Watts 2015a,b). The plate has a non-linear moment curvature relation provided by a YSE model. The non-linear differential equation is solved using an iterative spectral method (Garcia et al. 2015)

2 FLEXURE MODELLING APPROACH

2.1 Physical Model

The physical model consists of a thin elastic plate of variable flexural rigidity $D(x, y)$ floating on a fluid substrate. The substrate has the same density ρ_m as the upper mantle, and the plate is overlain by ocean having density of ρ_w. The differential equation describing the deflection of the plate $w(x, y)$ in response to a spatially variable vertical load $p(x, y)$ is given by

$$\nabla^2 \left[D\nabla^2 w\right] - (1-\nu)\left[\frac{\partial^2 D}{\partial x^2}\frac{\partial^2 w}{\partial y^2} - 2\frac{\partial^2 D}{\partial x \partial y}\frac{\partial^2 w}{\partial x \partial y} + \frac{\partial^2 D}{\partial y^2}\frac{\partial^2 w}{\partial x^2}\right] - N_x\frac{\partial^2 w}{\partial x^2} - 2N_{xy}\frac{\partial^2 w}{\partial x \partial y} - N_y\frac{\partial^2 w}{\partial y^2} + (\rho_m - \rho_w)gw = p(x, y), \quad (1)$$

where g is the acceleration of gravity and N_x, N_{xy}, and N_y are the in-plane forces. The equation follows the formulation in Ventsel & Krauthammer (2001) for plates with varying rigidity, but with the term for the substrate response adapted for the oceanic lithosphere. When the flexural rigidity $D(x, y)$ is uniform or varies smoothly, it can be expressed in terms of an elastic thickness $T_e(x, y)$,

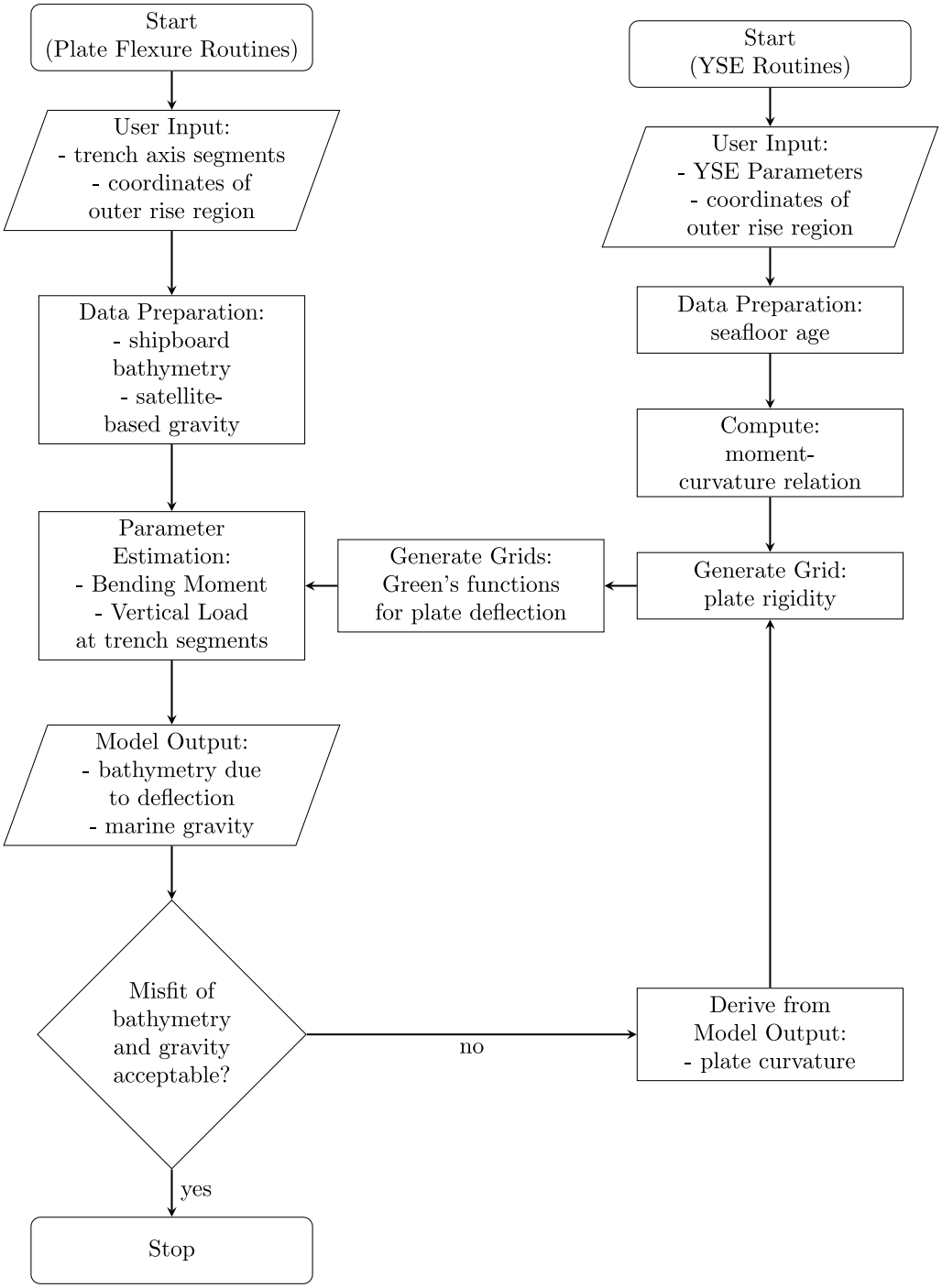

Figure 2. Flowchart of parameter estimation process for flexure modelling

$$D(x,y) = \frac{ET_e^3(x,y)}{12(1-\nu^2)}. \tag{2}$$

in which E is Young's modulus, and ν is Poisson's ratio.

We solve the equation using an iterative spectral method (Garcia et al. 2015) where the geographic

extent of the model is much larger than the geographic extent of the vertical load. The boundary conditions are such that the plate deflection and its derivatives vanish far from the loads.

Bending moments and vertical loads are applied along finite-length curved segments as shown in Fig. 1. The moment is approximated as a force couple of equal and opposing vertical loads following the numerical method described in Garcia et al. (2015). In addition to computing the deflection of the plate, the gravity anomaly is calculated by upward continuation of the seafloor gravity to the ocean surface using the mean depth in the region. Each curved segment serves as a Green's function for the model inversion. The regional trench model consists of multiple segments placed end-to-end following the planform of the actual trench. Let us assume that we had correct values for the strength of the moments and vertical loads along the specified number of segments. We begin the solution by constructing a spatially variable rigidity using the age of the lithosphere outboard of the trench (Müller et al. 2008, 2016) and a YSE model. A plate with a low rigidity of $\sim 10^{21}$ N·m is used for the model region inboard of the trench which represents the area covered by the overriding plate to complete the spatial definition of rigidity needed for the solver. Using the approach of Garcia et al. (2015) we solve for the plate deflection, gravity anomaly, and plate curvature for this initial guess at rigidity. We then use the curvature grid to re-estimate the spatial variations in rigidity by applying the YSE formulation. We iterate until convergence of the solution for the deflection of the plate (Burov & Diament 1995), which is normally reached after 5-10 iterations. This analysis provides linearized Green's functions for each of the segments. These Green's functions are used in the inversion to update the estimates of the moments and vertical loads along the segments. Curvature from the updated solution is used to re-estimate the spatial variations in rigidity and a second set of Green's functions is constructed. This outer loop generally converges after 3-5 iterations. Our iterative modelling procedure is depicted as a flowchart in Fig. 2.

2.2 Data Preparation

The inversion for the moments, vertical loads and outer trench wall deformation is performed by minimising the misfit between the model bathymetry and gravity. There are four types of data that go into this analysis. The coordinates of the trench planform are determined using the deepest points along the trench from Bassett & Watts (2015a,b), which are then divided into segments of a set length. The segments for two example areas are shown as dashed white lines in Fig. 3. The age of the lithosphere for the region is based on the analysis of Müller et al. (2008) and, as described above, lithosphere inboard of the trench is set to a low value of rigidity to simulate a weak subducted plate that will have little influence on the flexure of the plate outboard of the trench. Seafloor depth is based on a recent

global compilation at 500 m resolution (Olson et al. 2014) and gravity is based on a recent analysis by Sandwell et al. (2014).

The features of our model setup which are selected by the user include the length of the individual trench segments, the along-trench extent to be considered for load estimation, and the area of the observations to be included in the parameter estimation process (Fig. 3). For this work, we chose to divide the trench axis into 50-km long trench segments and estimate the loads for 500-km long regions in the along-trench direction. From the centre of this entire model region we measure a 300-km long sub-region along the trench axis and only include data that are approximately 750 km seaward of this smaller sub-region. The trench-parallel and trench-perpendicular extent of the data are about the same size as the trench-segment bins used for analysis in a previous study (Hunter & Watts 2016).

We processed the marine gravity and bathymetry data prior to inverting for the flexural parameters to generate the input seafloor gravity and topography data. First, we removed a long-wavelength slope based on the expected seafloor subsidence due to lithosphere cooling with age (Parsons & Sclater 1977) from the bathymetry data, and then did the same for the corresponding effect on the gravity data. We computed a spherical harmonic model for the free-air gravity anomaly to degree and order 16 and subtracted that from the marine gravity as well (Hunter & Watts 2016). Another correction varying slowly across large spatial scales is that due to sediment loading, which we also apply to the bathymetry data (Divins 2003; Whittaker et al. 2013). Short-wavelength features in both the bathymetry and gravity which we do not wish to fit in our models include seamount edifices and the seafloor offsets across fracture zones. Previous methods for isolating this non-flexural topography (Zhang et al. 2014) may take into account variations in crustal thickness, or alternatively, these features may be extracted through expert interpretation (Crosby & McKenzie 2009). However, we excluded these unwanted features by creating masks based on the parameters from a seamount location and geometry database (Kim & Wessel 2011), a fracture zone trace compilation (Wessel et al. 2015; Matthews et al. 2011), and a digital map of present-day large igneous provinces Coffin et al. (2006).

2.3 Estimating Model Parameters

We solve a parameter estimation problem for the values of bending moment and vertical shear force at the trench axis (Fig. 1) using a 1-norm minimisation. For every i-th trench segment, we solve for a downward vertical load V_i and a bending moment M_i that is applied perpendicular to that segment. In addition we impose a smoothness constraint to minimise the difference in moment and downward force between adjacent segments. The 1-norm minimisation is

$$\min \left\{ \|\mathbf{Am} - \mathbf{b}\|^1 + \alpha \|\mathbf{Sm}\|^1 \right\}, \tag{3}$$

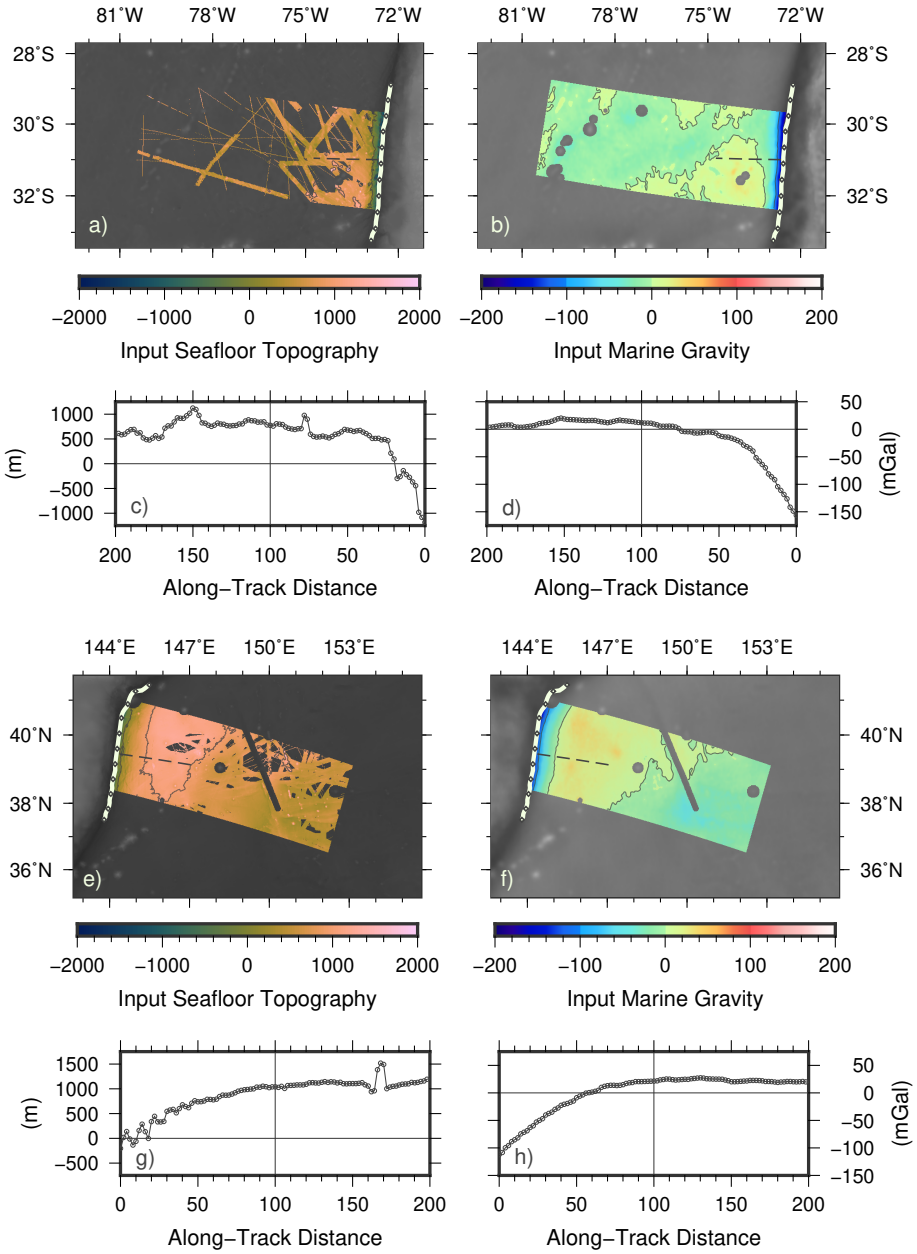

Figure 3. Sample data for input into trench flexure models (upper - Chile, lower - Japan). The coloured regions highlight the seafloor topography and marine gravity data. The white line segments drawn along the trench axes represent the loading segments for which free parameters of bending moment and vertical load are estimated. Seafloor topography and gravity profiles perpendicular to the trench are also shown. The input seafloor topography is taken from the residual of the bathymetry and estimates of the effects of subsidence due to plate cooling as well as sediment loading. The input gravity anomalies do not include long wavelengths of the gravity field in excess of around 2500 kilometres. For both input data sets, various topographic features such as seamounts, fracture zones, and large igneous provinces were edited out based on published data sets. (See main text for further details).

where $\mathbf{m}$ is a vector of model parameters, $\mathbf{A}$ is the design matrix, $\mathbf{b}$ is a vector of data constraints, $\mathbf{S}$ is the smoothing matrix and α is the relative weight given to the smoothing parameter. We set up a system of linear equations to jointly satisfy the relations $\mathbf{Am} = \mathbf{b}$ and $\mathbf{Sm} = \mathbf{0}$. These equations can be expressed in matrix form as,

$$\begin{bmatrix} \boldsymbol{\Gamma}_{\hat{w}}\mathbf{G}_w(M) & \boldsymbol{\Gamma}_{\hat{w}}\mathbf{G}_w(V) & \boldsymbol{\Gamma}_{\hat{w}} & \mathbf{0} \\ \lambda\boldsymbol{\Gamma}_{\Delta\hat{g}}\mathbf{G}_{\boldsymbol{\Delta}\mathbf{g},\mathbf{M}} & \lambda\boldsymbol{\Gamma}_{\Delta\hat{g}}\mathbf{G}_{\boldsymbol{\Delta}\mathbf{g},\mathbf{V}} & \mathbf{0} & \lambda\boldsymbol{\Gamma}_{\Delta\hat{g}} \\ \alpha_M\mathbf{D} & \mathbf{0} & \mathbf{0} & \mathbf{0} \\ \mathbf{0} & \alpha_V\mathbf{D} & \mathbf{0} & \mathbf{0} \end{bmatrix} \begin{bmatrix} \mathbf{m}_M \\ \mathbf{m}_V \\ w_0 \\ \Delta g_0 \end{bmatrix} = \begin{bmatrix} \boldsymbol{\Gamma}_{\hat{w}}\hat{\mathbf{w}} \\ \boldsymbol{\Gamma}_{\Delta\hat{g}}\boldsymbol{\Delta}\hat{\mathbf{g}} \\ \mathbf{0} \\ \mathbf{0} \end{bmatrix}. \tag{4}$$

On the left-hand side of eq. (4), the Green's functions $\mathbf{G}$ are calculated for the plate deflection w and gravity anomaly Δg that correspond to the model plate's flexural response to a unit bending moment M and unit vertical load V at the i-th model trench segment. The data vector $\mathbf{b}$ consists of subvectors for the processed bathymetry $\hat{w}$ and marine gravity anomaly Δg. The components of the model vector represent the estimated values of the applied loads at the N trench segments:

$$\mathbf{m}_M = [M_1, M_2, \cdots M_n]^T, \tag{5}$$

$$\mathbf{m}_V = [V_1, V_2, \cdots V_n]^T. \tag{6}$$

Along with these main flexural loading parameters, we also estimate an unknown offset w_0 between the processed bathymetry data and the model deflection surface, which is calculated in reference to the depth of zero deformation. The offset Δg_0 serves the same purpose for gravity anomalies.

On the right-hand side of eq. (4), the input data are comprised of independent sets of shipboard soundings and satellite altimetry-derived gravity anomalies. The observations to be compared with the model predictions are the bathymetry and marine gravity anomaly data after the corrections have been applied, and these inputs are represented in the sub-vectors $\hat{\mathbf{w}}$ and $\boldsymbol{\Delta}\hat{\mathbf{g}}$, respectively. The elements of these sub-vectors are assigned individual weights based on distance from the trench (Levitt & Sandwell 1995; Emry et al. 2014). These weights are expressed as the following diagonal matrices:

$$\boldsymbol{\Gamma}_{\hat{w}} = [\Gamma_{\hat{w},1}, \Gamma_{\hat{w},2}, \cdots \Gamma_{\hat{w},q}]^T, \tag{7}$$

$$\boldsymbol{\Gamma}_{\boldsymbol{\Delta}\hat{\mathbf{g}}} = [\Gamma_{\Delta\hat{g},1}, \Gamma_{\Delta\hat{g},2}, \cdots \Gamma_{\Delta\hat{g},r}]^T. \tag{8}$$

The smoothness constraint imposed on $\mathbf{m}_M$ and $\mathbf{m}_V$ may be adjusted independently through the choice of (α_M) and (α_V) values. The first-difference operator $\mathbf{D}$ is just

$$\mathbf{D} = \begin{bmatrix} 1 & -1 & 0 & \cdots & \cdots & 0 \\ 0 & 1 & -1 & 0 & \cdots & \vdots \\ \vdots & \ddots & \ddots & \ddots & \vdots & \vdots \\ \vdots & \vdots & \ddots & \ddots & \ddots & 0 \\ \vdots & \vdots & \cdots & 0 & 1 & -1 \end{bmatrix}. \tag{9}$$

As for the smoothing parameters, we prescribe a minimum value of α such that all vertical shear loading values estimated at the trench are applied in the downward sense, and all the bending moments have the same sign. Meanwhile, an upper bound on α would result from the case in which all segments have the same direction and magnitude of loading parameters – an over-smoothed model.

We can define a joint misfit function ψ for bathymetry and gravity as follows:

$$\psi = \frac{1}{1+\tilde{\lambda}} \left\{ \sum_{i=1}^{q} \left| \frac{\xi_{w_i}}{\zeta_w} \right| + \tilde{\lambda} \sum_{j=1}^{r} \left| \frac{\xi_{\Delta g_j}}{\zeta_{\Delta g}} \right| \right\}, \tag{10}$$

which is similar to the misfit criterion used in Levitt & Sandwell (1995). The residuals ξ at each model and data grid point (x, y) are computed using

$$\begin{aligned} \xi_{w_i} &= \Gamma_{w_i}\{w(x_i, y_i) - \hat{w}_i\} \\ &= \frac{1}{\Gamma_{w_i}} \left\{ \left[\sum_{k=1}^{n} \left(M_k G_{w,i}(M_k) + V_k G_{w,i}(V_k) \right) + w_0 \right] - \hat{w}_i \right\}, \end{aligned} \tag{11}$$

$$\begin{aligned} \xi_{\Delta g_j} &= \frac{1}{\Gamma_{\Delta g_j}} \{\Delta g(x_j, y_j) - \Delta \hat{g}_j\} \\ &= \Gamma_{\Delta g_j} \left\{ \left[\sum_{k=1}^{n} \left(M_k G_{\Delta g_j}(M_k) + V_k G_{\Delta g_j}(V_k) \right) + \Delta g_0 \right] - \Delta \hat{g}_j \right\}. \end{aligned} \tag{12}$$

The residuals are divided by ζ, which is the total absolute deviation from the mean,

$$\zeta_{\Delta h} = \sum_{i=1}^{q} \Gamma_{w_i} \left| \hat{w}_i - \bar{w} \right|, \tag{13}$$

$$\zeta_{\Delta g} = \sum_{j=1}^{r} \Gamma_{\Delta g_j} \left| \Delta \hat{g}_j - \Delta \bar{g} \right|, \tag{14}$$

and so the misfit measure is an indicator of how much of an improvement over a constant plane the model deflection surface provides in terms of fitting the data. A weighting parameter $\tilde{\lambda}$ controls the relative importance of the gravity to the bathymetry. Note that increasing $\tilde{\lambda}$ would tend to improve the model fits to gravity at the expense of the bathymetry residuals. For most cases the lowest misfit

Table 1. Physical Constants Used in Flexural Rigidity modelling

Description	Quantity	Value
E	Young's modulus	1.0×10^{11} Pa
ν	Poisson's ratio	0.25
L	thermal plate thickness	125 km
T_s	temperature at seafloor	0°C
T_L	temperature of upper mantle at base of plate	1350°C
κ	thermal diffusivity	8.0×10^{-7} m^2 s^{-1}
C_p	high-T ductile flow law stress constant	7.0×10^{-14} Pa^{-3} s^{-1}
C_d	low-T ductile flow law strain rate constant	5.7×10^{11} s^{-1}
σ_d	low-T ductile flow stress constant	8.5×10^9 Pa
Q_p	olivine activation energy, high-T	523 kJ/mol
Q_d	olivine activation energy, low-T	543 kJ/mol
n	power law exponent, high-T	3.0
$\dot{\varepsilon}$	strain rate	10^{-16}

values occur when $\tilde{\lambda}$ is between 0.1 and 1. We set $\tilde{\lambda} = 0.8$ for our suite of models since this value minimised the misfit values for a series of tests that we performed.

The rigidity grid for each of our thin elastic plate models is estimated using a non-linear moment-curvature relation that assumes a brittle-elastic-plastic rheology for the oceanic lithosphere (Fig. 4). In this yield strength envelope formulation (Goetze & Evans 1979; McNutt & Menard 1982), the differential stress in the upper portion of the lithosphere is assumed to be limited by brittle yielding. At greater depths, brittle failure transitions into ductile yielding. Moreover, the ductile behavior is separated into regimes of low- and high-temperature plasticity. In the middle of the plate where the stresses do not reach these brittle and ductile yielding values, the plate continues to behave elastically and the stresses linearly increase away from the nodal plane with a gradient equal to the plate curvature. Note that unlike the case for flexure profile modelling, the horizontal grid dimensions in our models may not necessarily be aligned with two of the principal stress axes, which is the implicit assumption when dealing with profiles that only have one horizontal dimension. Strictly speaking, a coordinate transformation should be applied so that the curvature from the model grid can be put into the expressions for differential stress.

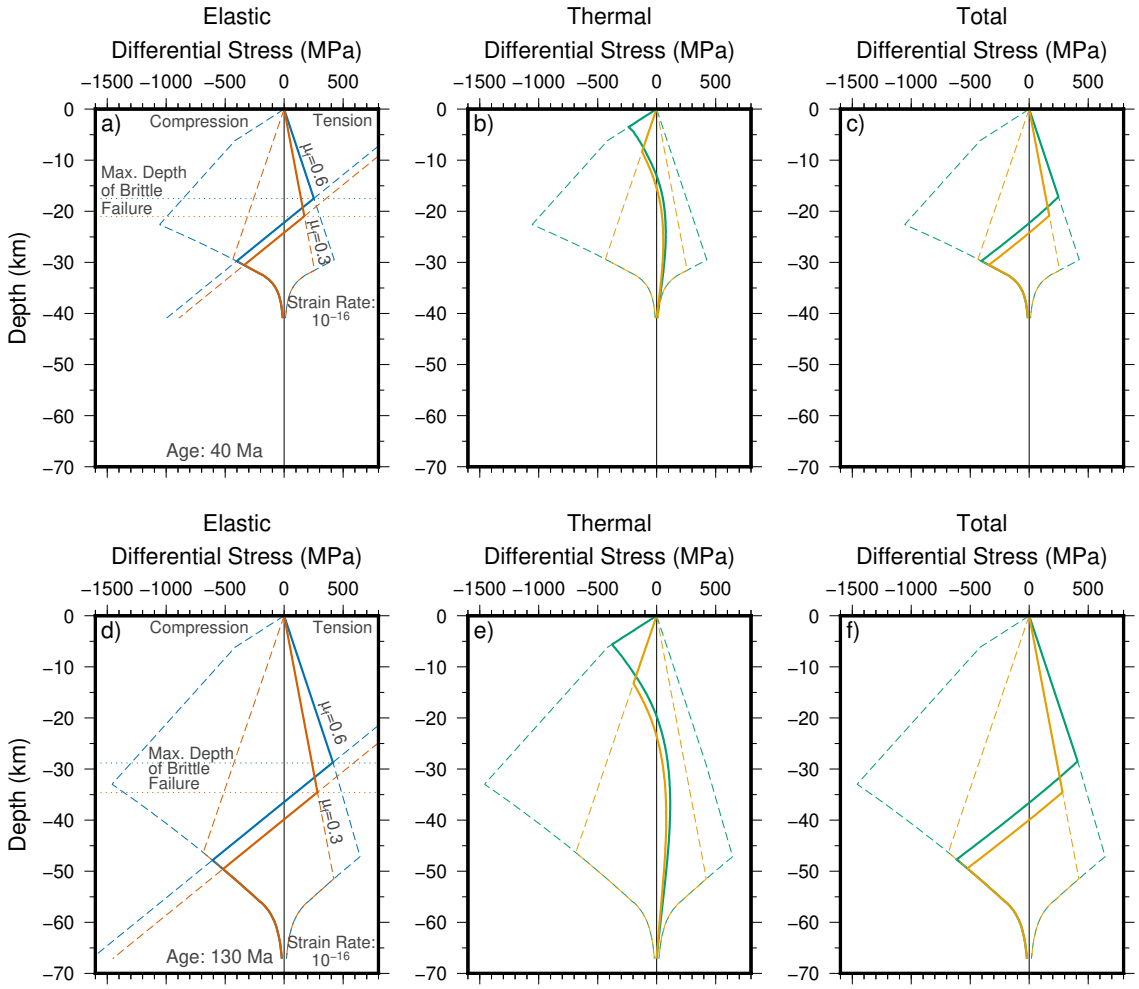

Figure 4. These plots show differential stress as a function of depth within the limits imposed by a yield strength envelope (YSE). The parameters for the YSEs used in the calculations only differ in the values of the static coefficient of friction μ_f for the brittle failure criteria. One model uses μ_f=0.85 at shallow depths, which then transitions to μ_f=0.6 at greater depths (Byerlee 1978) (referred to in the text as the S model). The other model (referred to in the text as the W model) uses a low value of μ_f=0.3. (Craig et al. 2014b). Both models assume that the pore pressure is fully hydrostatic. At the bottom of the lithosphere, the yield strength is determined by a set of low-temperature and high-temperature ductile flow laws with parameters that are appropriate for dry olivine (Mueller & Phillips 1995). The geotherms are calculated using a plate cooling model (Parsons & Sclater 1977). Subfigures a-c display the results for young lithosphere (40 Ma), while subfigures d-f are for old lithosphere (130 Ma). The plots in a) and d) show the differential stress profiles for elastic plate bending when the magnitude of the concave-downward curvature is 5 x 10^{-7}. The depth of brittle yielding is at the intersection of the elastic stress and the brittle yielding curve. Meanwhile, b) and e) show the accumulated thermal stress (Wessel 1992). The total stress after combining the contributions from both components can be seen in c) and f).

2.4 Lithosphere Strength and Flexural Stresses

For the portion of the YSE describing brittle behavior, we used a frictional failure criterion based on rock deformation experiments (Byerlee 1978). The shear strength τ along a fault plane is related to the normal stress σ_n, and the pore-fluid pressure P_f by

$$\begin{aligned} \tau &= 0.85(\sigma_n - P_f), \qquad \sigma_n \leq 200 \text{ MPa}, \\ \tau &= 0.6(\sigma_n - P_f) + C_0 \quad \sigma_n > 200 \text{ MPa}. \end{aligned} \tag{15}$$

In the above case the coefficient of friction μ_f has a value of 0.85 in shallow regions, but at depth $\mu_f = 0.6$. We set the rock cohesion C_0 at 50 MPa. We also ran models which were cohesionless and had a low value of friction ($\mu_f = 0.3$, Craig et al. 2014a), such that for all values of σ_n, we used the following relation:

$$\tau = 0.3(\sigma_n - P_f). \tag{16}$$

For the results we present in this paper, we assumed a pore fluid pressure that was fully hydrostatic.

At the greater depths and higher temperatures of the lower lithosphere, deformation occurs mainly through ductile flow. We followed the formulation in Goetze & Evans (1979) for the low-temperature flow law but used parameter values from Mueller & Phillips (1995), and these are listed in Table 1. That flow law relating the strain rate $\dot{\varepsilon}$ to the differential stress σ has the following form:

$$\dot{\varepsilon} = C_d \sigma \left\{ -\frac{Q_d}{RT} \left[1 - \left(\frac{\sigma}{\sigma_d} \right) \right]^2 \right\}, \quad \sigma > 200\,\text{MPa}. \tag{17}$$

Following Mueller & Phillips (1995), we set the transition between low-temperature and high-temperature ductile behaviour when the differential stress is at 200 MPa. The high-temperature ductile flow law we used is in a power law form, and has a value for the activation energy that lies within the range of experimental values for dry olivine (Mueller & Phillips 1995), but adjusted to achieve continuity with the low-temperature flow law, or in other words, to ensure that for a given strain rate and temperature, both flow laws will predict the transition value for differential stress.

$$\dot{\varepsilon} = C_p \sigma^n \exp\left(-\frac{Q_p}{RT} \right), \quad \sigma < 200\,\text{MPa}. \tag{18}$$

The magnitude of the ductile yield strength computed from these flow laws is thus dependent on the geotherm. To compute the temperature distribution, we used the plate cooling model of Parsons & Sclater (1977). A compilation of the physical constants used in constructing the yield strength envelopes is provided in Table 1.

For purely elastic plates, the components of stress σ along the x and y directions within the plate depend on the distance z' from the nodal plane,

$$\begin{aligned}
\sigma_{xx} &= -\frac{E}{1-\nu^2} z' \left(\frac{\partial^2 w}{\partial x^2} + \nu \frac{\partial^2 w}{\partial y^2} \right), \\
\sigma_{yy} &= -\frac{E}{1-\nu^2} z' \left(\frac{\partial^2 w}{\partial y^2} + \nu \frac{\partial^2 w}{\partial x^2} \right), \\
\tau_{xy} &= -\frac{E}{1+\nu} z' \left(\frac{\partial^2 w}{\partial x^2} + \nu \frac{\partial^2 w}{\partial x \partial y} \right).
\end{aligned} \tag{19}$$

Thus, if a solution for the values of w are found for a particular flexure problem, the stresses within the plate can be computed. Note, however, that when applying the limits imposed by a choice of YSE parameters, the stress components first have to be projected onto the principal stress axes.

For half of the models that we present in this work, we also included the thermal stresses in the computation of differential stresses within the model lithosphere (Wessel 1992). Varying amounts of thermal contraction due to the cooling history of the oceanic lithosphere leads to the accumulation of thermal stresses. These stresses have two main components: an average contraction stress that is independent of depth, and a depth-varying component which we refer to as the thermal bending stress. To compute the cooling rates, we used a plate cooling model (Parsons & Sclater 1977), so the derivative of the temperature with respect to time t at a given lithosphere age t_a and depth d from the plate surface is given by

$$\frac{\partial T(t_a, d)}{\partial t} = \frac{-2T_L \pi \kappa}{L^2} \sum_{n=1}^{\infty} n \sin\left(\frac{n\pi t_a}{L}\right) \exp\left(\frac{-n^2 \pi^2 \kappa t_a}{L^2}\right), \tag{20}$$

in which T_L is the temperature of the mantle at the base of the plate, κ is the thermal diffusivity, and L is the plate thickness. The thermal stress increments $\Delta\sigma_{x'x'}$ along the main principal stress axis x' are related to the changes in temperature by

$$\Delta\sigma_{x'x'} = -\frac{\alpha_l E}{1-\nu} \Delta T(t_a, d). \tag{21}$$

The thermal stress profile with depth is then calculated by integrating these thermal stress increments over all time steps up to the current age. For a fully elastic plate, this can be approximated by a straightforward sum of the values evaluated at each time step. However, if the stresses are limited by a YSE, then the stresses in excess of the yield values must be truncated after applying the increment to the already accumulated stresses. Finally, the value of the constant thermal contraction stress must be adjusted such that the integral of the thermal stress profile over the thickness of the plate results in no net in-plane force acting on the plate.

In calculating the superposition of the thermal stress and the elastic bending stresses, we follow the general procedure outlined in Mueller et al. (1996) for evaluating inelastic stresses when limited by a YSE after a loading sequence. First, the accumulated thermal stress profile for the lithosphere at a given age is calculated, and this is considered as a residual stress field that precedes the response of the plate to loads at the trench axis. Our model is not dynamic in the sense that we did not trace the evolution of these stresses from seaward of the outer rise to the trench outer slope. Instead, for a certain value of curvature at a location within the plate that has a certain age, the elastic bending stresses are assumed to increment upon the pre-existing thermal stresses, while fulfilling the relevant condition for net in-plane forces, which is that the integral of the total stress profile within the plate vanishes. As this condition on the integral might not be immediately met after the addition of the stresses and the subsequent truncation of the resulting sum under the YSE, a constant stress offset may need to be further added or subtracted to the previously mentioned thermoelastic, elastic, and inelastic stress components. We solve for this offset in an iterative manner (Mueller et al. 1996).

The specific form of the governing equation for plate flexure as shown in eq. (1) was not derived by taking into account the thermoelastic stress from the beginning. A key difference in the fundamental physical assumptions is that in purely elastic bending the nodal plane is assumed to be a surface undergoing no vertical strain, but if a plate does not have a uniform steady-state temperature distribution within it, then that assumption may not hold for the depth variation of the strain from thermal contraction. If the linear coefficient of thermal expansion α_l is constant, and the displacements along the nodal plane of the plate can be written in terms of independent components along x and y, then the strain components from thermoelastic and purely elastic stresses may be superimposed linearly. In that case, a thermal equivalent bending moment M_T may be defined (Ventsel & Krauthammer 2001),

$$M_T(x,y) = \alpha_l E \int_{-H/2}^{H/2} T(x,y,z) z dz, \tag{22}$$

in which H is the mechanical thickness of the plate, and z is the distance from the nodal plane. With this definition, the only modification needed for eq. (1) to be applied to thermoleastic bending is an additional term on the right hand side as follows,

$$p_T(x,y) = -\frac{1}{1-\nu}\nabla^2 M_T(x,y). \tag{23}$$

This may be interpreted to mean that in order to include the effect of thermoelastic stresses in plate bending, a correction term that depends on the temperature field must be applied to the vertical load distribution $p(x,y)$. In practice, for the seafloor age distributions in the trench outer rise and slope regions which we considered in our models, the magnitude of this correction is such that it only

results in additional flexural deflections on the scale of several metres. As will be elaborated upon in the Discussion section, the main effect of the thermoelastic pre-stress is to delay the onset of the outer rise fractures that are observed as horst and graben structures on the outer trench wall.

In summary, we consider 4 models for the yield strength and thermoelastic pre-stress in our inversions (Fig. 4). All models have hydrosatic pore pressure to reduce the normal stress in the brittle layer. All models also use the Parsons & Sclater (1977) thermal structure. The ductile yield criterion is based on the Goetze & Evans (1979) model using the parameter values and strain rate of 10^{-16} s^{-1} from Mueller & Phillips (1995). There are two strong models (μ_f = 0.6) - without and with thermoelastic pre-stress, and we'll call these the S-model and S-T-model, respectively. There are two weak models (μ_f = 0.3) - without and with thermoelastic pre-stress, and we'll call these the W-model and W-T-model, respectively. As shown in the next section, the strength of the brittle layer has an effect on the shape of the flexure, especially at the outer trench wall, and that the W-model provides better fits to the bathymetry and gravity data.

3 RESULTS

The S and S-T models provided satisfactory fits to the gravity and bathymetry data. However, in general the S-models underestimated the peaks of the topography and gravity of the outer rise while also overestimating the depth and gravity in the vicinity of the trench axis and outer trench wall (Fig. 6b and f, 7b and f). We can improve the fits to the data by lowering the coefficient of friction (W and W-T models) as seen in (Fig. 6 d and h, 7 d and h). Based on this misfit analysis we favor the W-models but cannot distinguish between W and W-T models from the deflection modelling alone.

The W model results for all the trench regions are summarized in Table 2. The first column is the subduction zone sub-region ID and these are labeled on Fig. 5. The next few columns contain the central coordinates of the trench outer slope for each sub-region, the average seafloor age (Müller et al. 2008, 2016) and misfit values for all of the bathymetry and gravity data in each of the model sub-regions. Most of these values are less than 0.5, indicating that the flexure models perform at least 50% better than a flat plane in fitting either the bathymetry or gravity observations. The average improvement for the gravity data of 0.32 is greater than the average fit to the topography of 0.45 because the gravity lacks some of the small scale noise present in the topography due to the effect of smoothing by upward continuation. Examples of these residuals are shown in Fig. 6 g, h and Fig. 7 g, h.

The remaining columns of Table 2 contain values for the other model quantities that are computed from the flexural deflection w, such as the the bending moment M, curvature C, effective elastic thickness T_e, and the mean seafloor depth. Example maps for some of these quantities are shown for

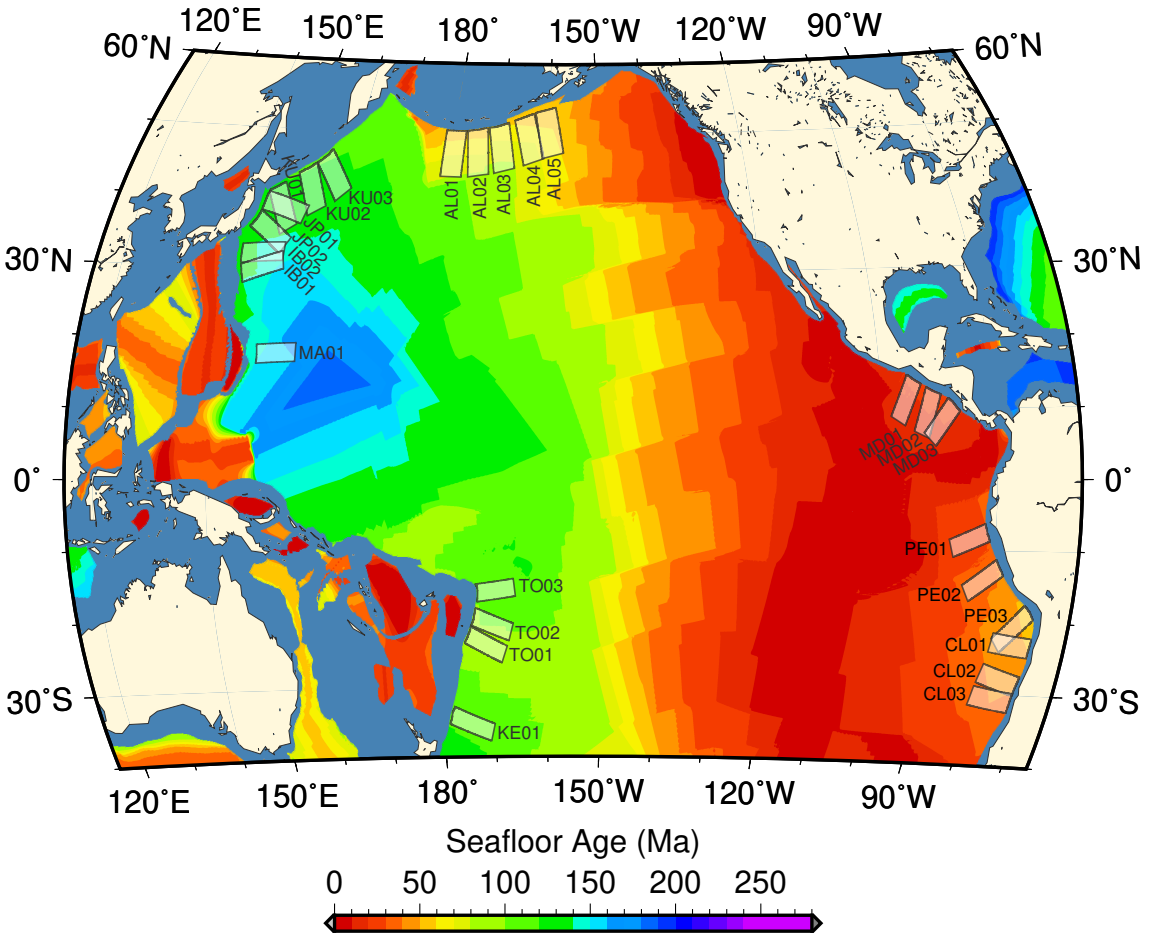

Figure 5. Map of subduction zone sub-regions (solid grey boxes) and seafloor age based on magnetic anomalies (Müller et al. 2016, 2008). Each sub-region extends approximately 300 kilometres along the trench axis and 750 kilometres away from it. Further details are given in the main text.

a region offshore NE Japan (Fig. 8) and offshore south Chile (Fig. 9) in the case of the W set of models. The values as listed in Table 2 have been calculated to summarize the results for each region as follows. First, the curvature of the model deflection was calculated from the second derivatives of w. Then, closely spaced trench-perpendicular profiles were constructed, and the location of the point with the greatest magnitude of curvature at the trench outer slope was identified. Finally, the mean of these curvature values was computed. The locations of these points are shown in Fig. 8b and Fig. 9b as red dotted lines for the NE Japan and south Chile model regions, respectively. The individual bending moment values were calculated across the same locations as those used for the curvature by integrating the product of the differential stress σ and the distance from the nodal plane over the thickness of the model plate. If we define a vertical coordinate axis z' which is oriented normal to the surface of plate, and where the origin is placed at the nodal plane, this integral can be written as,

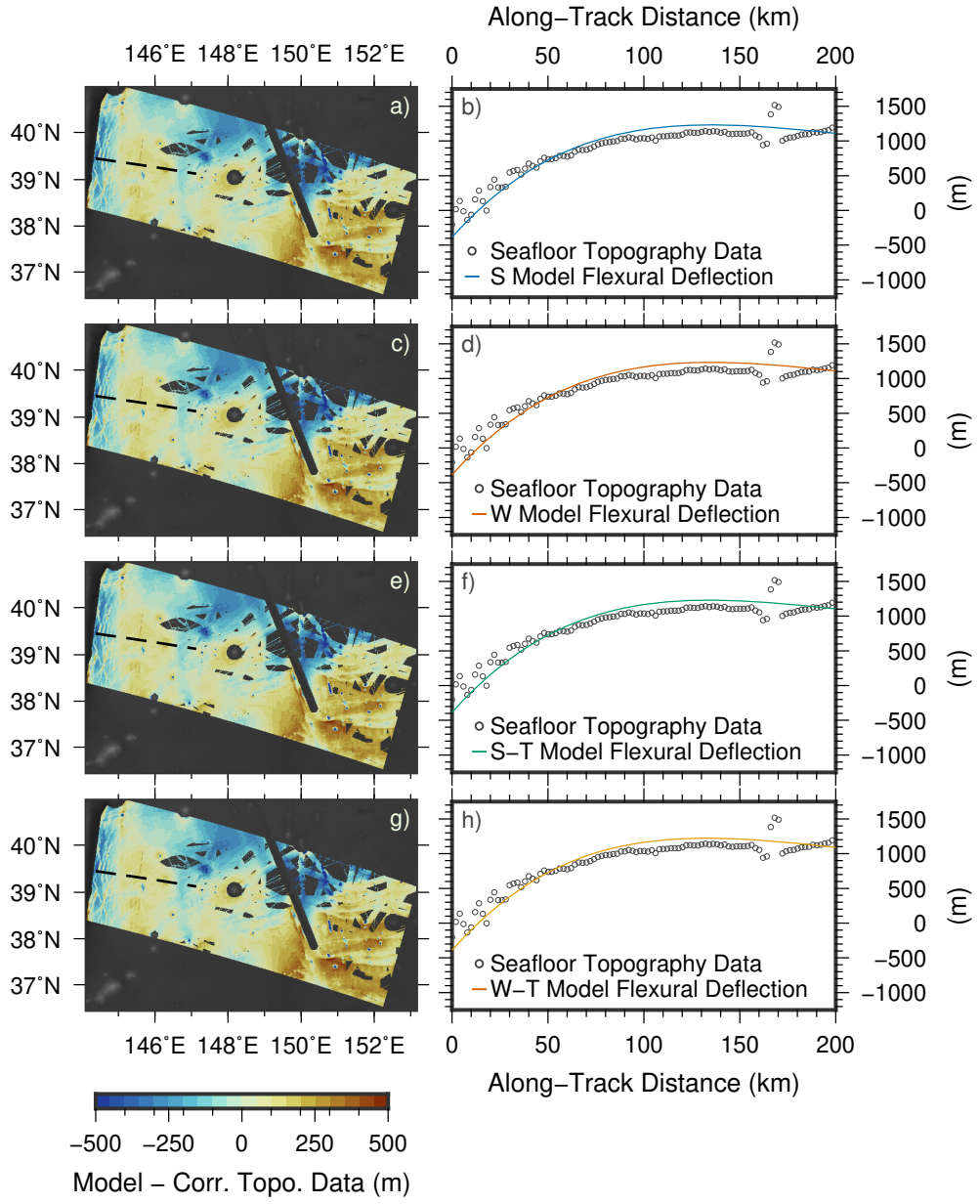

Figure 6. For a region offshore NE Japan (ID: JP02), the residuals between the model flexural deflection and the seafloor topography data are shown for four different model setups depending on the value of the coefficient of friction and whether the effect of thermal stress was included (see text). Profiles of model fits for each case are also shown, with points for the data and a solid line for the model result. The sampling track is displayed as a dashed line in each map.

$$\int_{-T_m+d_n}^{d_n} \sigma z' dz'. \tag{24}$$

Here, d_n is the distance from the top of the plate to the nodal plane. The flexural rigidity is calculated

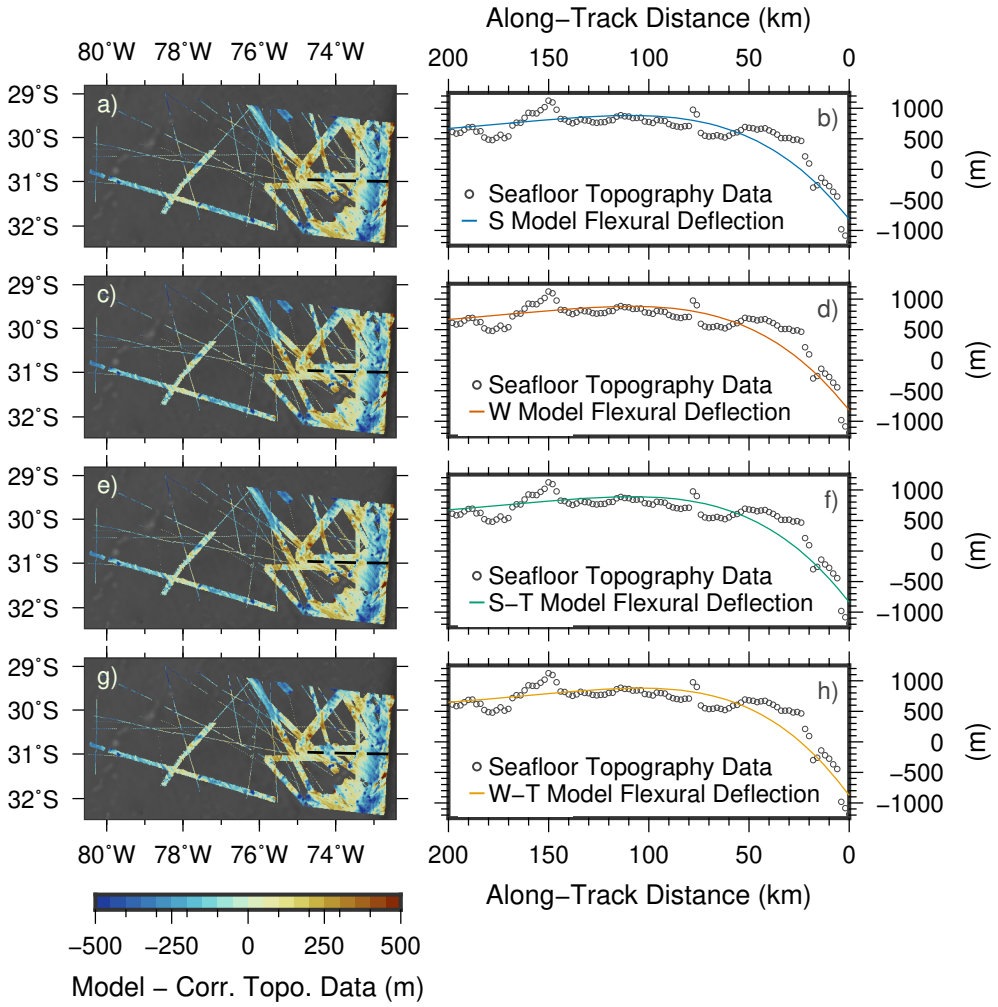

Figure 7. For a region offshore south Chile (ID: CL03), the residuals between the model flexural deflection and the seafloor topography data are shown for four different model setups depending on the value of the coefficient of friction and whether the effect of thermal stress was included (see text). Profiles of model fits for each case are also shown, with points for the data and a solid line for the model result. The sampling track is displayed as a dashed line in each map.

from the slope of the moment-curvature relation and is then converted to effective elastic thickness so that the values can be compared with isotherms. The reported elastic thickness values in Table 2 are also for the points of highest concave-downward curvature on the trench outer slope. Lastly, we also provide estimates for the mean depth level of the unbent plate, which we later compare against predictions of seafloor subsidence from the thermal model. This depth offset is calculated by applying the model deflection offset resulting from the parameter inversion process to the original bathymetry data within the model region, then taking the average across all data points except for those excluded by the topographic feature masks.

We now proceed to use these model parameters to make inferences about the thermo-mechanical

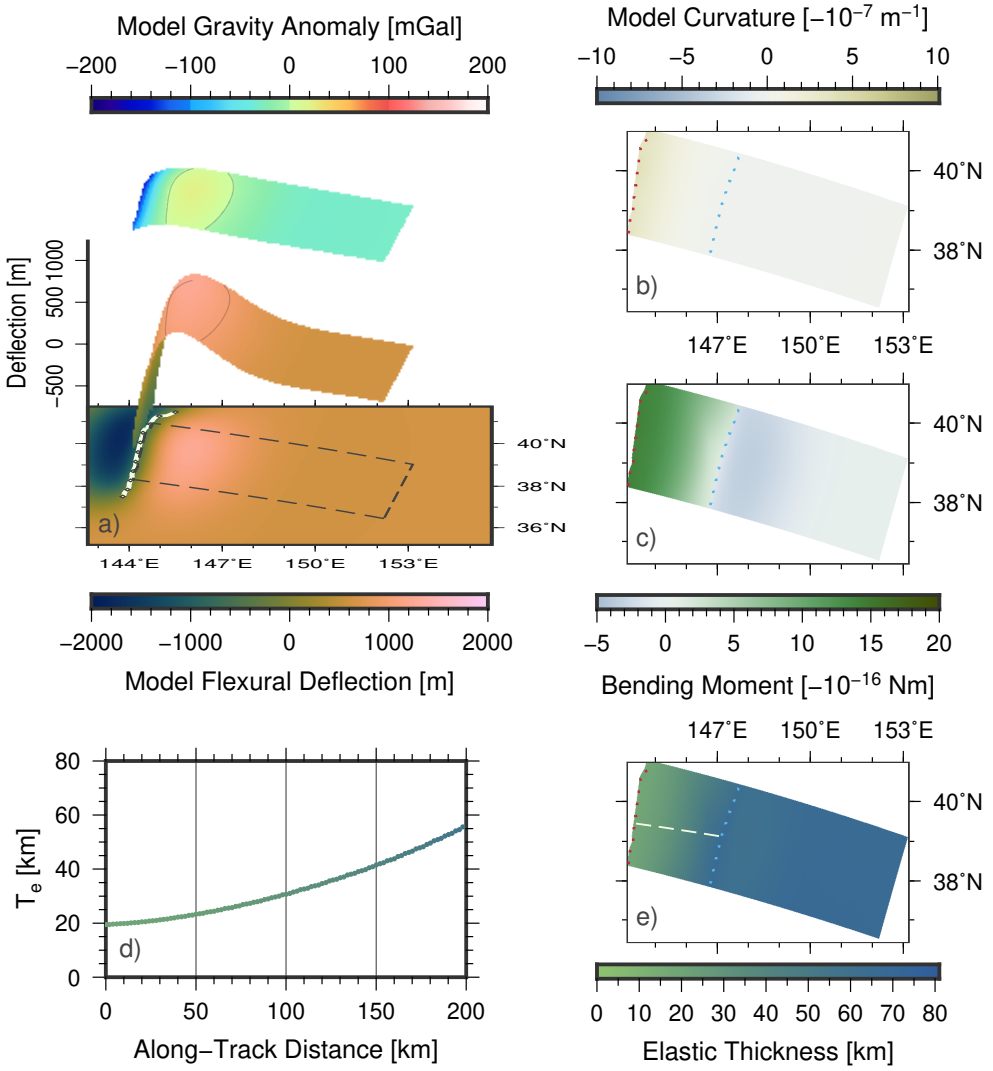

Figure 8. For a region offshore NE Japan (ID:JP02) and using the W lithosphere rheology, a map of the original model output for the deflection w and a 3-D visualization of the best-fit flexural surface selected are shown in a). Also displayed in a) is the expected marine gravity anomaly Δg as calculated from w. The contours are drawn every 1000 m for w and every 200 mGal for Δg. From w, the curvature as seen in b) is computed. The red dotted line marks the locations of the largest magnitudes of the curvature at the trench outer slope, while the blue dotted line traces the smallest magnitudes of the curvature just seaward of the outer rise. In turn, the curvature is used to compute the bending moment as seen in c). The elastic thickness values T_e are then obtained from the moment-curvature relation which is specific to the W set of models. Subfigure d) shows a trench-perpendicular profile of T_e, the location of which is shown in relation to the model region mapped in subfigure e).

properties of incoming lithosphere at circum-Pacific subduction zones. Fig. 10a shows the average bending moment versus age sampled at the same locations as the points of the largest magnitude of curvature on the trench outer slope. This includes results for the S (blue solid circles), S-T (green outlined circles), W (orange solid circles), and W-T (yellow outlined circles) models. We compare

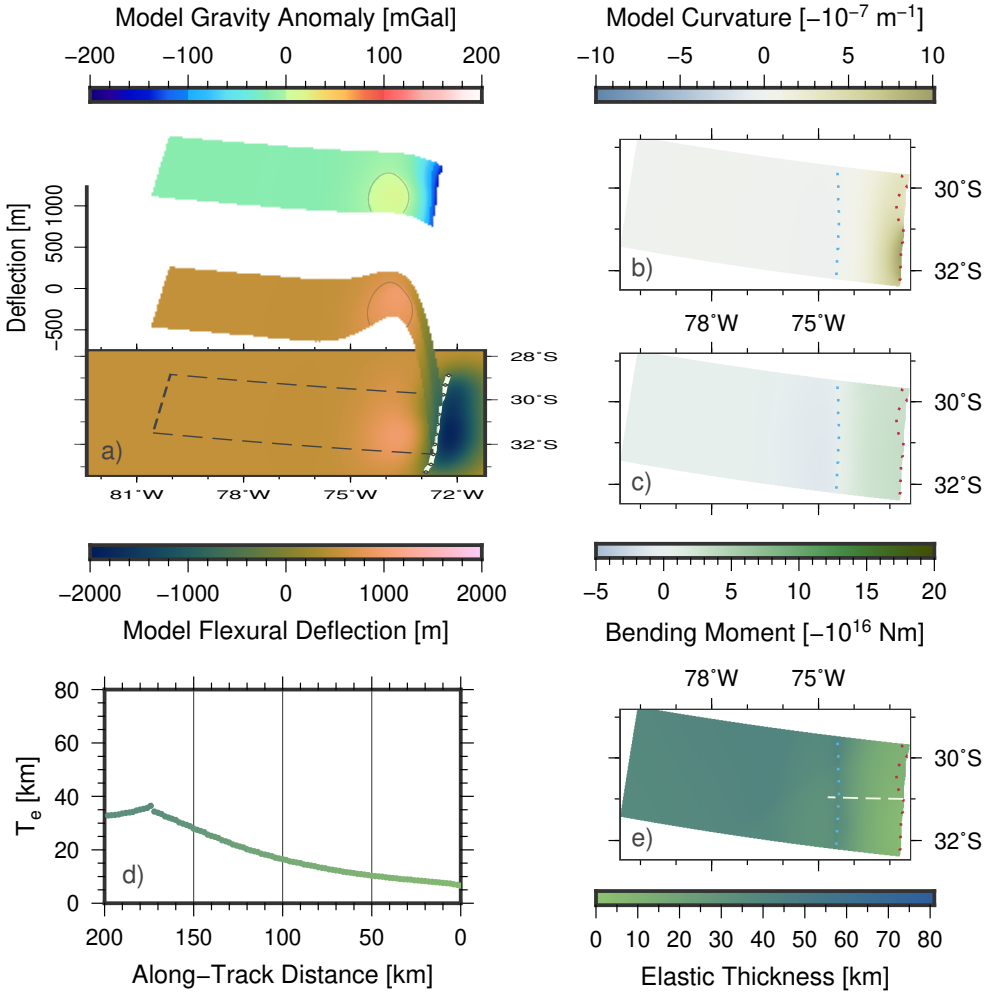

Figure 9. For a region offshore south Chile (ID:CL03) and using the W lithosphere rheology, a map of the original model output for the deflection w and a 3-D visualization of the best-fit flexural surface selected are shown in a). Also displayed in a) is the expected marine gravity anomaly Δg as calculated from w. The contours are drawn every 750 m for w and every 150 mGal for Δg. From w, the curvature as seen in b) is computed. The red dotted line marks the locations of the largest magnitudes of the curvature at the trench outer slope, while the blue dotted line traces the smallest magnitudes of the curvature just seaward of the outer rise. In turn, the curvature is used to compute the bending moment as seen in c). The elastic thickness values T_e are then obtained from the moment-curvature relation which is specific to the W set of models. Subfigure d) shows a trench-perpendicular profile of T_e, the location of which is shown in relation to the model region mapped in subfigure e).

these estimated moments to the corresponding saturation moment curve (solid black line for both S and S-T models, and a dashed black line for both W and W-T model). The value of saturation moment depends on the value of the friction coefficient, with the weaker value of friction having a corresponding lower saturation moment. We found that the results do not depend on whether the

thermal pre-stress is included. The saturation moment serves as a strict upper bound for the values of moment that the plate can support. Our results show that young lithosphere ($<$ 70 Ma) is nearly moment saturated at the trench outer slope, while old lithosphere ($>$ 70 Ma) is at least 2/3 moment saturated.

An estimate for the the reference seafloor depth at which the flexural deflection is zero was determined by calculating the mean seafloor depth within the model region after the addition of the estimated constant model offset. This calculated reference depth is then compared with the average seafloor age at the trench outer slope in Fig. 10b. Also shown is the depth-age relation predicted by the Parsons & Sclater (1977) thermal subsidence model. In general the zero-deflection depth is well fit by the model even at very old ages around 140 Ma. Much of the seafloor in these areas was not included in previous seafloor subsidence depth compilations because they are in areas "contaminated" by trench flexure so these new estimates can be used for additional depth versus age modelling although we have yet to explore further how subtle tilts across both longitude and latitude are affecting our depth estimates. Unlike in Bry & White (2007) or Levitt & Sandwell (1995), we did not include a slope in the bathymetry or gravity observations as a free parameter in our modelling approach, and there might be some small trade-off between a plane tilt either in the trench-normal or trench-perpendicular direction, and the average depth offset.

We compare in Fig. 10c how our effective elastic thickness (T_e) estimates vary among the subduction zones we considered and also across the different rheology models. In Hunter & Watts (2016), their parameter estimation process resulted in two constant values for T_e along each of the trench-perpendicular profiles in their study: a higher "seaward" value for the region around the outer rise and further away from the trench, as well as a lower "landward" value which was the final value for T_e as the model plate approached the trench. The transition between these "seaward" and "landward" values was given by a ramp-like function instead of a step change as in other work (Contreras-Reyes & Osses 2010; Zhang et al. 2014). Therefore, to enable some form of comparison between our results and those in Hunter & Watts (2016), we sampled the T_e for each of our plate flexure sub-regions by finding the locations of the lowest trench-perpendicular curvature on the outer rise (analogous to "seaward" T_e) and also the highest magnitudes of trench-perpendicular curvature at the outer slope close to the trench (analogous to "landward" T_e). The locations of these "outer rise" and "outer slope" points are plotted in Fig. 8e and Fig. 9e as blue and red dotted lines, respectively. The corresponding mean T_e values for the outer rise and outer slope are shown in Fig. 10c, with the rheology models being designated by the various symbol colours.

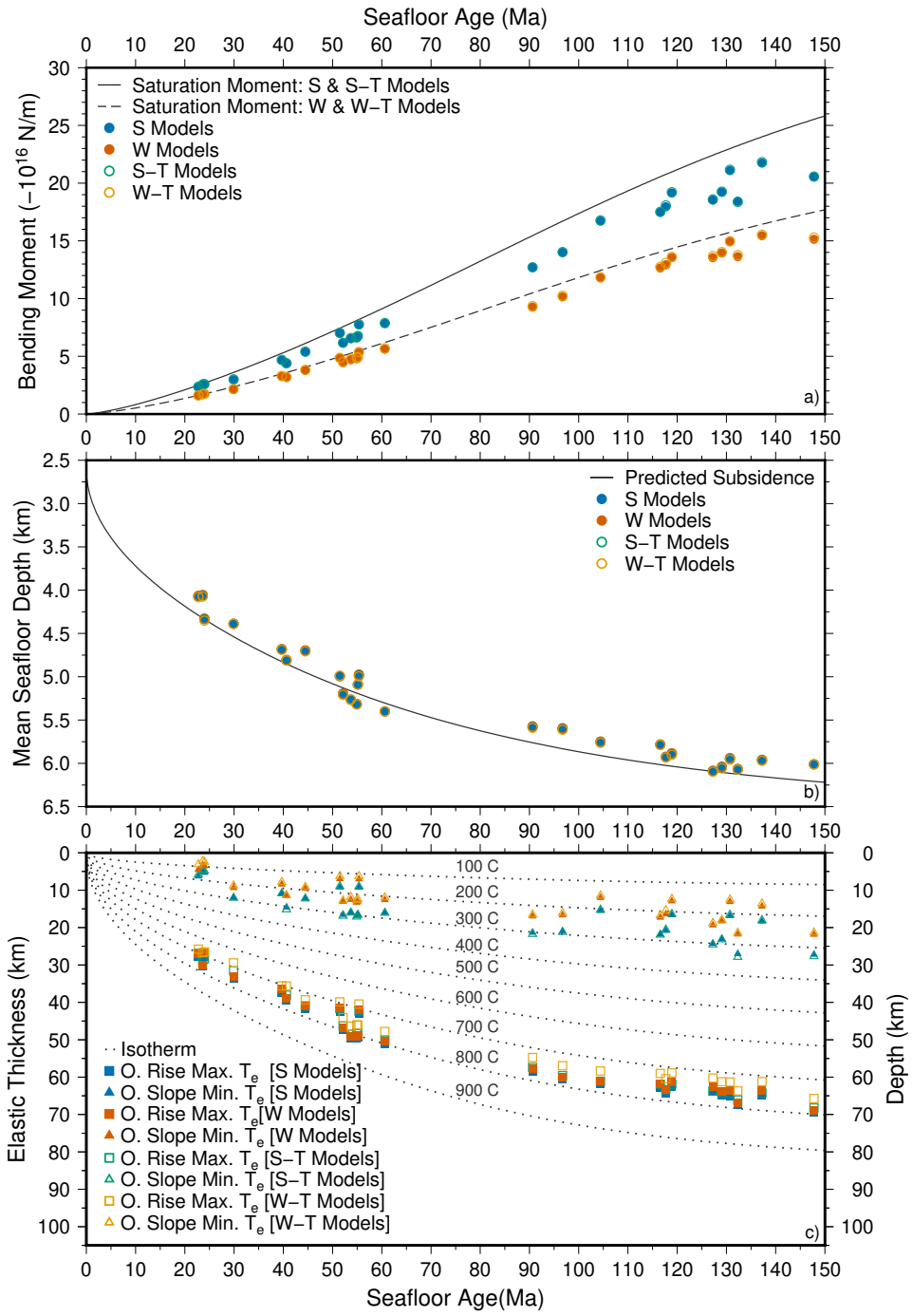

Figure 10. The model results (in diamond symbols) are plotted against seafloor age at the trench outer slope for the following quantities: a) bending moment, and b) seafloor depth offset. The elastic thickness estimates (T_e) in c) are mean values at the trench outer slope and the back of the outer rise (for example, along the red dotted lines in Figs. 8e and 9e, and the blue dotted lines in Figs. 8e and 9e, respectively). There is a clear increase in the bending moment with age that is limited by the saturation moment given by the specified plate rheology.

Table 2. Results Summary for Averaged Quantities at the Trench Outer Slope for the W Model

Sub-Region ID	Midpoint along Trench Lon (deg.)	Midpoint along Trench Lat (deg.)	Seafloor Age (Ma)	Misfit Measure w	Misfit Measure Δg	Bending Moment $\bar{M}$ (-10^{16} N)	Deflection Curvature $\bar{C}$ (-10^{-7}/m)	Elastic Thickness $\bar{T}_e$ (km)	Seafloor Depth Offset (km)
MD01	-94.02	14.20	22.73	0.41	0.31	1.58	-11.33	4.50	-4.07
MD02	-90.66	12.54	23.63	0.42	0.28	1.69	-14.07	3.27	-4.06
MD03	-87.09	10.63	23.97	0.48	0.28	1.72	-13.95	3.50	-4.33
PE01	-81.44	-7.38	29.90	0.47	0.39	2.12	-4.34	9.36	-4.39
CL03	-72.55	-31.06	39.70	0.44	0.34	3.26	-6.81	8.42	-4.68
PE02	-78.76	-12.33	40.65	0.48	0.36	3.17	-3.90	11.54	-4.81
CL02	-72.18	-28.76	44.47	0.58	0.32	3.78	-5.51	9.50	-4.70
CL01	-71.33	-23.45	51.49	0.42	0.34	4.83	-9.18	6.97	-4.99
AL05	-161.02	53.45	52.12	0.40	0.23	4.46	-3.63	13.06	-5.19
AL01	-179.73	50.36	53.71	0.50	0.38	4.70	-4.10	12.53	-5.27
AL02	-175.12	50.58	54.91	0.52	0.37	4.79	-3.73	13.28	-5.31
AL04	-165.46	52.44	55.15	0.48	0.26	4.86	-3.81	12.97	-5.09
PE03	-72.44	-18.44	55.36	0.38	0.35	5.33	-9.44	7.02	-4.97
AL03	-170.70	51.17	60.62	0.79	0.30	5.62	-4.33	12.57	-5.40
TO01	-174.21	-22.34	90.63	0.48	0.39	9.26	-3.45	16.94	-5.57
TO02	-173.08	-19.80	96.71	0.47	0.33	10.15	-3.67	16.64	-5.59
TO03	-172.33	-16.33	104.41	0.40	0.35	11.80	-6.27	11.99	-5.75
KE01	-178.05	-33.91	116.56	0.55	0.35	12.65	-3.88	17.27	-5.78
KU03	154.07	46.18	117.70	0.52	0.37	12.93	-4.24	16.35	-5.92
KU02	151.18	44.47	118.90	0.26	0.22	13.55	-6.07	12.91	-5.88
KU01	145.92	41.65	127.24	0.33	0.26	13.54	-3.39	19.35	-6.09
JP02	144.31	39.64	129.06	0.30	0.20	13.95	-3.72	18.27	-6.04
IB02	142.12	32.06	130.71	0.40	0.23	14.92	-6.10	13.09	-5.94
JP01	143.41	37.01	132.30	0.49	0.34	13.63	-2.83	21.78	-6.06
IB01	142.86	29.19	137.22	0.39	0.27	15.45	-5.53	14.29	-5.96
MA01	147.77	17.82	147.77	0.42	0.53	15.14	-2.94	21.85	-6.01

4 DISCUSSION

4.1 Lithospheric Strength Versus Age

The material comprising oceanic lithosphere has fairly uniform composition due to its formation at seafloor spreading ridges, and its thermal history is mainly governed by plate cooling as it moves

away from these ridges towards subduction zones. Therefore, the mechanical behavior of oceanic lithosphere should depend mainly on its temperature (McKenzie et al. 2005). Compilations of surface heat flow measurements (Hasterok et al. 2011), and ocean depth related to thermal subsidence (Parsons & Sclater 1977; Hillier & Watts 2005) show a clear dependence on lithosphere age. These suggest that plate cooling models with age dependence can be used to infer mechanical strength via some choice of temperature-dependent rheology. However, if the incoming plate at a trench is modeled as having a uniform flexural rigidity, global estimates of the effective elastic thickness (Levitt & Sandwell 1995; Bry & White 2007) did not seem to support the conclusion of the lithosphere strength increasing with age. Attempts at explaining this apparent conflict have emphasized the role of inelastic yielding in the weakening of the plate at the trench outer slope (Wessel 1992; Bry & White 2007; Craig & Copley 2014). Evidence for stresses within the plate exceeding the elastic limit includes the prevalence of surface fractures in high-resolution bathymetry (Massell 2002; Mofjeld et al. 2004), dipping reflectors in seismic reflection profiles (Ranero et al. 2003; Boston et al. 2014), and the occurrence of earthquakes with normal fault mechanisms (Emry & Wiens 2015; Craig et al. 2014a).

In our modelling approach, we prescribe the initial elastic thickness by setting it to be equal to the mechanical thickness, which is the depth at which the ductile yield stresses decrease to some arbitrary threshold. In our case this limit is set to be at 1 per cent of the overburden pressure (Hunter & Watts 2016; Cloetingh & Burov 1996). Since the ductile yield stresses are related to temperature, the mechanical thickness should increase with age, and depending on the plate cooling model selected there is a correspondence with a certain temperature value. As mentioned in previous sections, by iteratively computing curvatures the flexure models we use can calculate an updated plate rigidity. The results from our models demonstrate that a plate with a mechanical thickness which is initially dependent on age can undergo sufficient reduction in effective elastic thickness to fit the high deflection curvature in the observed bathymetry and gravity.

Furthermore, the models show that all subduction zones considered for this study are approaching moment saturation. Moreover, the model-estimated moment increases dramatically with age in parallel with the saturation moment.

4.2 Outer Rise Fracturing

As discussed above, the plate is nearly moment saturated at the trench axis, so the upper part of the plate, where strength is controlled by brittle fracturing, should have faults that extend from the surface to nearly 1/2 the plate thickness. With a few assumptions we can use the model to predict the vertical offset on the outer rise faults. The fracture model is shown in Fig. 11 where a plate of initial thickness H has a curvature of $\frac{\partial^2 w}{\partial x'^2}$, where x' is a horizontal coordinate axis along the direction of maximum

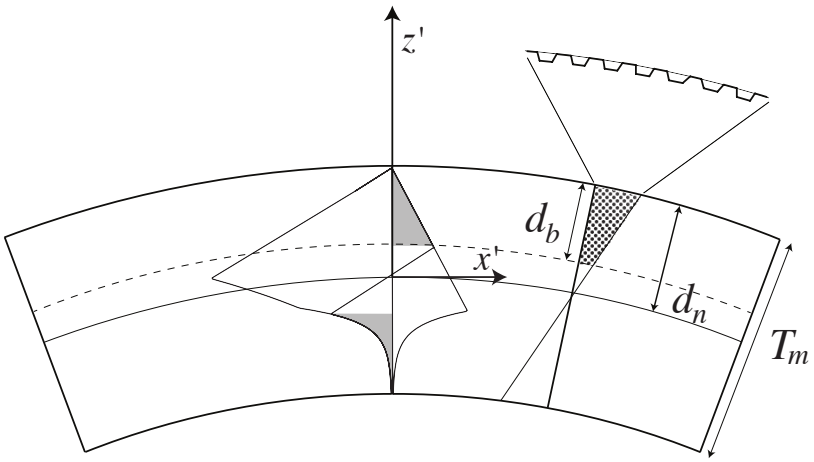

Figure 11. Schematic diagram showing a plate of thickness T_m that is bent beyond its elastic limit, with vertical coordinate z' and horizontal coordinate x'. According to the YSE formulation fractures will extend to a depth d_b. We assume the upper zone of inelastic deformation is incompressible (stippled). The depth-averaged extension in that zone is accommodated by faulting and graben formation on the surface.

curvature. The amount of strain ϵ is related to the curvature and the distance from the nodal plane by $\epsilon = -z' \frac{\partial^2 w}{\partial x'^2}$ (Turcotte & Schubert 2014). The strain is purely elastic near the nodal plane, but there is inelastic yielding in both the upper and lower portions of the plate where there is sliding on optimally oriented faults and ductile flow, respectively. We assume that these yielding regions are incompressible, so that horizontal extension in the upper brittle layer of depth d_b is accommodated by vertical deformation. The deformation will appear on the surface as down-dropped blocks (Fig. 11). The average vertical offset on the surface is then equal to the horizontal strain integrated through the thickness of the upper deformed layer. Following the same conventions as in eq. (24),

$$\Delta h = \frac{\partial^2 w}{\partial x'^2} \int_{d_n - d_b}^{d_n} z' dz'. \tag{25}$$

The result is

$$\Delta h = \frac{1}{2} \frac{\partial^2 w}{\partial x'^2} d_b (2d_n - d_b). \tag{26}$$

For a plate having an initial 50 km thickness, a faulting depth of 20 km and a typical magnitude of curvature of $4 \times 10^{-7} m^{-1}$, the vertical relief will be 120 m. If the ratio of undisturbed surface (horst) to down dropped blocks (graben) is $1/2$, then the vertical relief will be 240 m. Note that in the numerical plate bending calculation, the depth of the nodal plane is adjusted such that the integrated in-plane

stress is zero so it will not be exactly in position at the middle of the plate. Moreover, it is possible that a non-zero average value of in-plane stress will modify the depth and amplitude of the faulting. Thus the relief of the horst and graben on the outer trench wall will depend on plate curvature, the initial plate thickness, and the strength of the in-plane force, if any.

We can compare this model prediction with the amplitude of the horst and graben topography on the outer trench wall of the Japan and Chile trenches. We analyse the SRTM15_PLUS 15-minute digital bathymetry grid and apply the spectral averaging routines of Bassett & Watts (2015a,b) to remove the long-wavelength, trench-normal topography associated with the outer rise and the seaward wall of the trench. Residual bathymetry along the Japan trench is shown in Fig. 12b, and the order of magnitude reduction in dynamic range of the topographic grid improves the identification of horsts and grabens. The residual bathymetric grid is sampled along 150 km long trench-normal profiles. We then interpret two surfaces along the top of horst blocks and the base of grabens respectively (grey dashed line in Fig. 12a). The distance between these surfaces shows how the amplitude of the horst and graben topography varies with distance from the trench-axis. The proportion of grabens is estimated from the proportion of the residual bathymetric profile that is below the mid-point of the horst and graben surfaces.

Fig. 13a shows a sequence of residual bathymetric profiles taken over a 50 km wide region of the NE Japan trench centered on 39.5N. The dotted red profiles show the amplitude of horst and graben topography and the stack of these profiles is shown in Fig. 13b. This stack shows that outer rise faulting in this segment of the Japan trench begins at least 100 km from the trench-axis. The amplitude of horst and graben topography increases gradually to 100 m, 45 km from the trench-axis. Landward of this point the fault throw increases significantly and 400-500 m deep grabens are observed within 20 km of the trench axis. The solid red profile in Fig. 13b shows the fault throw predicted from our S model. This is close to the observed graben depth at distances $<$20 km from the trench, but is a factor $>$2 greater than the grabens $>$50 km away from the trench axis.

We have repeated this analysis for a segment of the South Chile subduction zone centered on 31°S. As shown in Fig. 14b, although the abyssal hill fabric in this region is pronounced, outer rise faults are visible in the residual SRTM15_PLUS bathymetry (Figure 14). In contrast to NE Japan, horsts and grabens are only well expressed within 45 km of the trench-axis (Fig. 15). This may suggest that outer rise fracturing does not extend further from the trench-axis, or that the smaller amplitude of faults in this region are being obscured by the pre-existing plate structure.

The mismatch between the S and S-T models for fault throw and the observed amplitude of the horst and graben topography close to the trench axis for the Japan and South America subduction zones potentially indicates that the observed normal faults could be accommodating more strain than

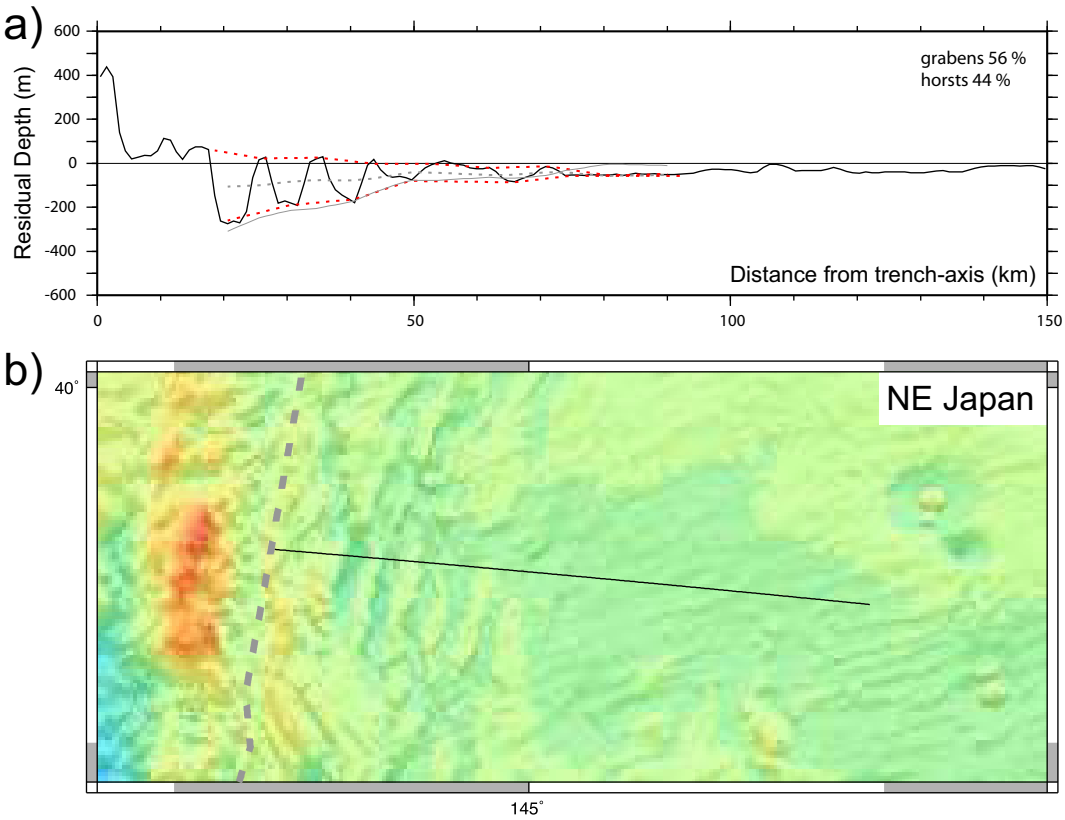

Figure 12. Outer rise fractures in NE Japan: a) Residual bathymetry across the seaward wall of the trench and outer rise. Dashed grey profiles traverse the top of horst blocks and the base of grabens. The distance between these surfaces (dotted red line) is used to estimate the depth of grabens. The dotted grey line is equidistant between the top (horst) and bottom (graben) surfaces and is used to estimate the proportion of horsts and grabens. b) Residual SRTM15_PLUS swath bathymetry. Dashed grey and solid black lines mark the trench-axis and the location of the profile shown in a) respectively.

inferred from our elastic-plastic formulation. The models for which the coefficient of friction is weak (W and W-T) are able to match the large fault throws more closely. However, for the models that use a strong friction coefficient and include the effect of thermal stress (S-T), there is an area further away from the trench over which the fault throws are low and only increase slightly, which then suddenly transitions to an area with much higher fault throw values that increase more rapidly. The observed fault throws display a similar behavior in that the fault scarps remain small in the residual bathymetry until about 100 to 50 kilometers away from the trench axis, at which point the fault throws start to increase.

We also note that despite the 90 Myr difference in the age of the subducting plate, the amplitude of horst and graben topography is comparable in both regions. The similarity in the amplitude of fault throws seems in contrast to the observed increase in seismogenic depth for earthquakes on the outer

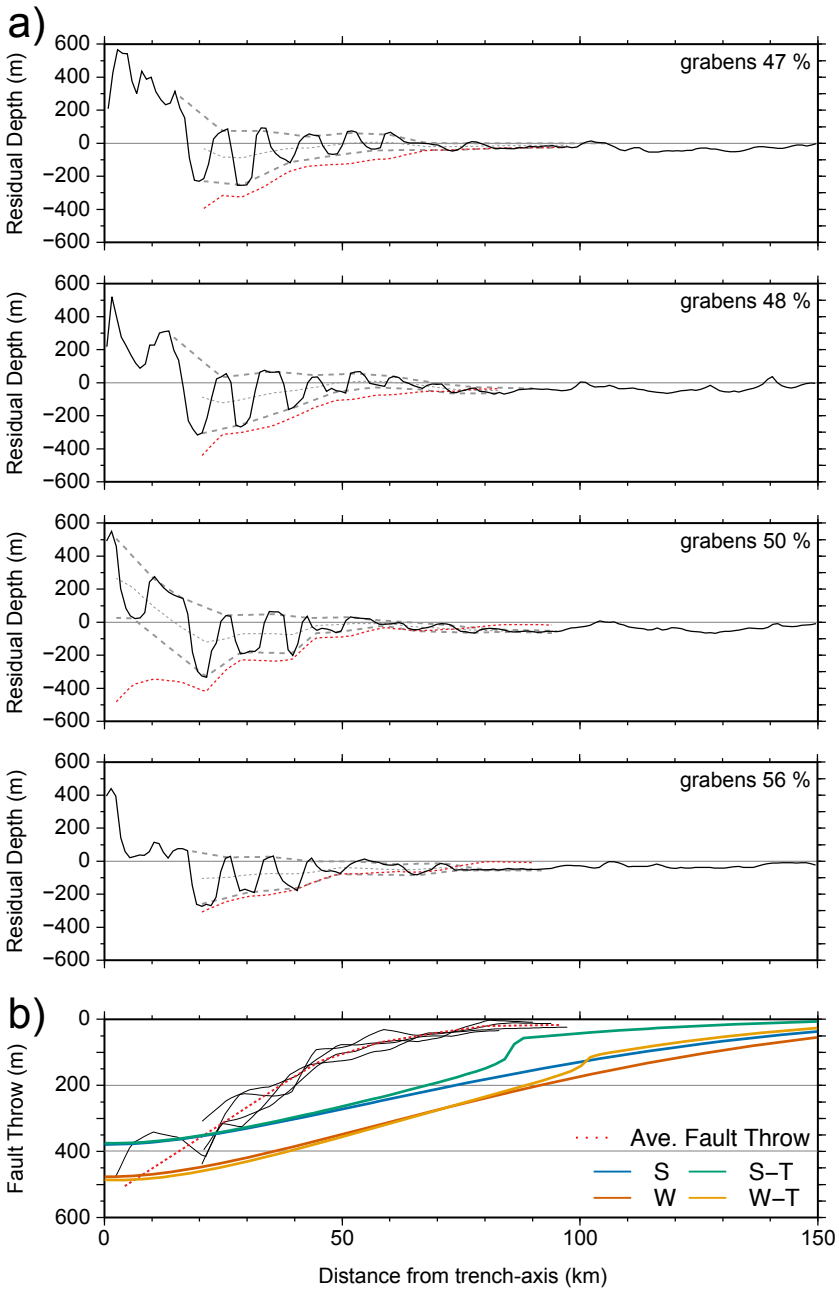

Figure 13. a) Profiles showing outer rise fractures in NE Japan between 39.5° N and 40° N. Figure nomenclature as in Fig. 12a. b) Stack of graben depths along-strike showing how the throw on normal faults increases toward the trench-axis. Dashed red line shows the average of these profiles. The estimated fault throws for the various sets of models are also plotted.

rise and slope (McKenzie et al. 2005; Craig et al. 2014a), therefore implying that normal faults of shallower depth extent do not necessarily produce less prominent surface fractures. However, this is not necessarily in conflict with our model since a smaller value of the depth of yielding d_b can be compensated for by a higher curvature to produce the same amount of predicted change in height Δh.

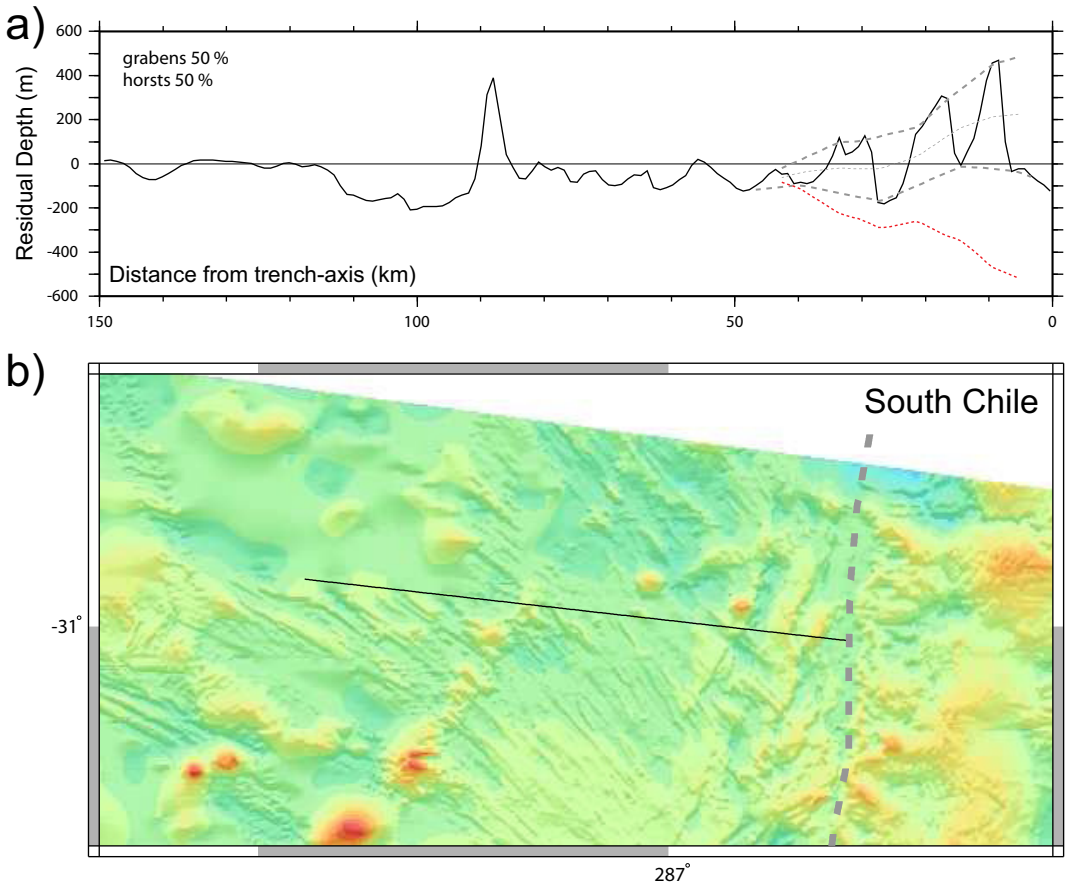

Figure 14. Outer rise fractures in S Chile: a) Residual bathymetry across the seaward wall of the trench and outer rise. Dashed grey profiles traverse the top of horst blocks and the base of grabens. The distance between these surfaces (dotted red line) is used to estimate the depth of grabens. The dotted grey line is equidistant between the top (horst) and bottom (graben) surfaces and is used to estimate the proportion of horsts and grabens. b) Residual SRTM15_PLUS swath bathymetry. Dashed grey and solid black lines mark the trench-axis and the location of the profile shown in a) respectively.

Furthermore, within the brittle zone the yield stresses are largely independent of temperature, so a dependence on age would not be obvious.

In another study concerned with the interpretation and analysis of several seismic reflection lines across the outer slope of the Japan trench (Boston et al. 2014), the authors suggest that while steady slip on older faults can accumulate to produce large offsets, the presence of small offset scarps suggest that fractures can continue forming on the plate surface as it approaches the trench. This may call the assumption of steady-state deformation on the trench outer slope into question.

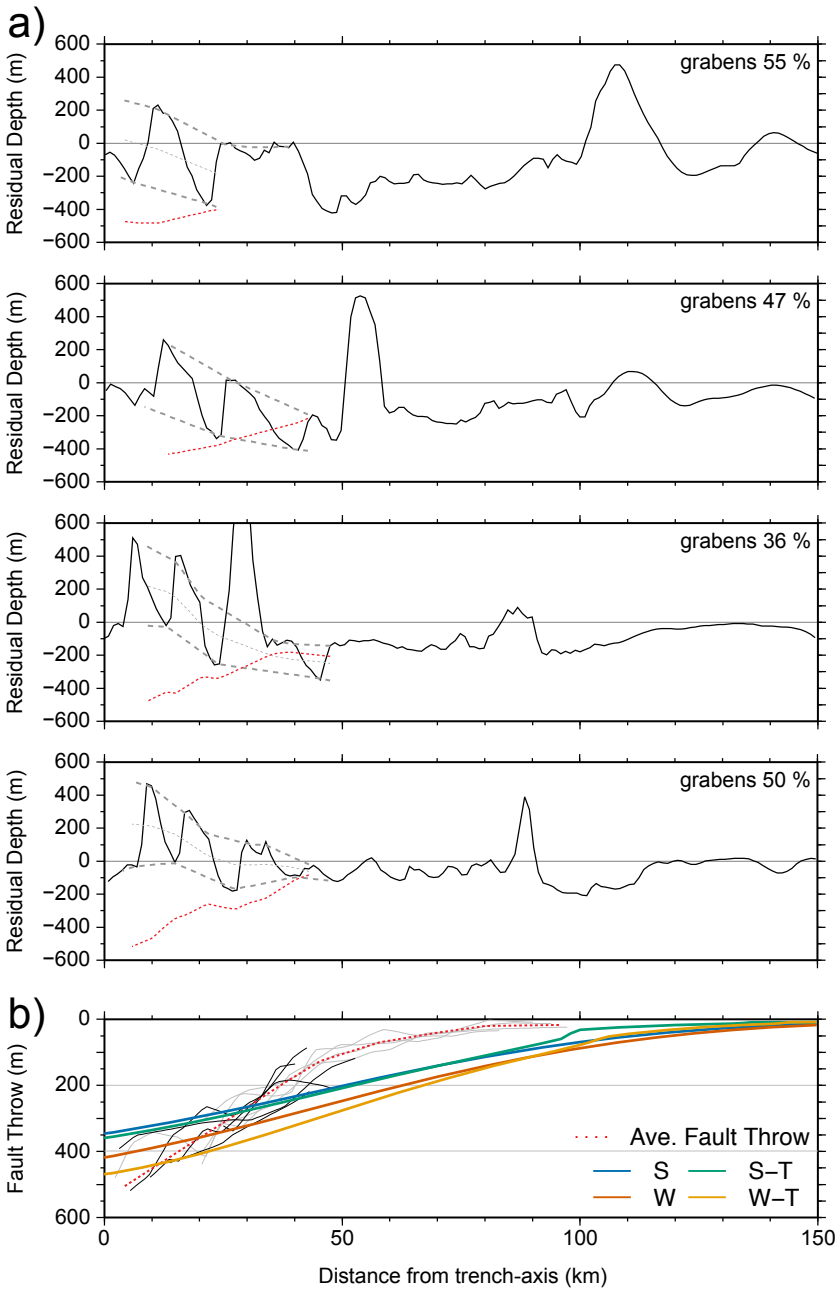

Figure 15. a) Profiles showing outer rise fractures in S Chile between 30° S and 31° S. Figure nomenclature as in Fig. 13a. b) Stack of graben depths along-strike showing how the throw on normal faults increases toward the trench-axis. The estimated fault throws for the various sets of models are also plotted as solid lines with the colors indicated by the legend. Black and light profiles are from S Chile and NE Japan respectively. The dashed red line is the average fault throw as in Fig. 13b. Despite significant differences in seafloor age, the throw on normal faults in S Chile is comparable to that observed in NE Japan.

4.3 Further Considerations

While the rheology parameters we selected to construct a suitable YSE for the flexure modelling produce satisfactory fits to seafloor depth and marine gravity, it may be possible to improve upon the results by conducting a systematic search of the parameters. We have used a combination of parameters in the YSE configuration that is unique to this work, but the individual values are still based on previously published numerical modelling or experimental work (Mueller & Phillips 1995; Craig et al. 2014a).

However, based on our preliminary tests, we concur with the conclusion of Zhong & Watts (2013) that altering parameters associated with the high-temperature ductile flow law (such as the activation energy Q_p or Q_d, stress constant C_p, or strain rate constant C_d) has a greater effect on the shape and curvature of the flexure surface than changing the coefficient of friction. Since the lower portion of the YSE determines the model mechanical thickness, this may imply that there is a range of initial elastic thickness values for undeformed lithosphere that eventually result in ideal fits after yielding occurs. A related concern in this regard is the choice of a thermal model, which would also increase or decrease the mechanical thickness. There are a few recent plate cooling models (McKenzie et al. 2005; Ritzwoller et al. 2004) which we did not examine in this work.

Also in Zhong & Watts (2013), the authors argue that a range of friction coefficient values from 0.25 to 0.7 while holding other parameters constant results in model misfits that are similar. From analysis of the strikes of new fractures and reactivated abyssal hills, Billen et al. (2007) propose that the friction coefficient is around 0.6, while from the study of focal mechanism dips, Craig et al. (2014a) infers a value of about 0.3. In our modelling we use a single set of YSE parameters and so do not take into account whether incoming seafloor fabric is being reactivated (for example, at the Middle America trench (Ranero et al. 2003)), or new fractures are being formed (for example at the Tonga trench (Massell 2002; Fan et al. 2016)). However, some regions appear more complicated because of a combination of these two styles of normal faulting, such as that observed in several offshore areas at the Japan and Izu-Bonin trenches (Kobayashi et al. 1998; Nakanishi 2011). Apart from the coefficient of friction, we have not considered the effect of changing the cohesion parameter. Reducing the fault cohesion linearly as the elastic strain accumulates (Zhou et al. 2015; Zhou & Lin 2018; Naliboff et al. 2013) could induce progressive weakening with increased curvature that is more pronounced than what our models are currently capable of generating, which might help improve our models of faulting.

A potential contribution of our fault modelling approach to geochemical and geodynamics studies of the Earth's interior is in predicting the extent of hydration for the incoming lithosphere at subduction zones (Faccenda et al. 2009). Understanding the water input at subduction zones has implications

for theories of the planetary hydrological cycle at geological time scales. Observations at the outer slope of the Middle America trench using seismic refraction (Van Avendonk et al. 2011) and marine electromagnetic imaging techniques (Naif et al. 2015) suggest the presence of water as pore fluid or hydrous minerals throughout the oceanic crust and perhaps the uppermost mantle. Similarly, models of seismic body-wave velocity (V_p) structure constructed using data from active-source surveys recorded on ocean bottom seismometer arrays have been used to infer hydration of the incoming plate at portions of the Alaska subduction zone (Shillington et al. 2015), as well as at the northern segment of the Japan Trench and the southern segment of the Kuril trench (Fujie et al. 2018). Output from numerical experiments illustrate that bending-related stresses allow seawater to penetrate downward along seafloor faults (Faccenda et al. 2009). Once within the lithosphere the water can be bound into mineral phases through chemical reactions such as serpentinisation. If simple assumptions are made connecting the seismogenic depth to the extent of hydration, the amount of water input carried by the into the upper mantle could be estimated (Emry & Wiens 2015). Once a method for validating our model predictions of faulting depth is tested, we can carry out a similar calculation and relate this to other constraints on the water content in the mantle.

5 CONCLUSIONS

We have extended previous efforts at modelling thin elastic plate flexure at subduction zones by incorporating inelastic effects and considering loads applied at the actual trench planform geometry. Our approach jointly fitted depth soundings and gravity data to variable rigidity flexural surface models at 26 sites around the Pacific basin. Traditional YSE models provide worse fits than our choice of modified parameters because they fail to capture the steep sudden descent of the plate at the trench outer slope simultaneously with the broad prominence of the outer rise. The preferred YSE has a weak friction, which results in the high curvatures at the trench outer slope that seem to be required by the observations. Most importantly, the estimated moment increases by a factor of 6 between the youngest and oldest lithosphere in excellent agreement with the strengthening versus age from the thermal models. All the plates are bent well beyond their elastic limit at the trench axis as required by subduction. As a consequence of our modelling approach which assumes an equivalence of the mechanical thickness with the initial elastic thickness of a point on the elastic plate with no deformation, the modelled strength of the oceanic lithosphere seaward of the outer rise prior to significant bending displays a dependence on seafloor age. Meanwhile, the distribution of effective elastic thickness values estimated for the trench outer-slope shows more variation and so the trend is not as apparent. For our preferred rheology that has a weak brittle layer, all lithosphere older than 80 Ma approach an effective elastic thickness of $\sim$ 20 km at the trench outer slope.

We used results from our model grids to calculate the vertical throw on the outer trench wall normal faults. A comparison with the actual vertical throw shows poor fits with the actual throw being up to 200 meters greater than the model prediction at the visible onset of faulting. This misfit suggests that perhaps future models incorporating a curvature-dependent strain-weakening mechanism could provide a better match to the outer trench wall fracturing.

6 ACKNOWLEDGEMENTS

We are grateful to Paul Wessel and Jeff Gee for their comments on an early draft of the manuscript. We also thank Wenyuan Fan, Zhitu Ma, and Diego Melgar for guidance on aspects of parameter estimation theory. The software implementation of the iterative spectral method was based in part on a routine written by Karen Luttrell (Luttrell & Sandwell 2012). The parameter estimation program was modified from a routine written by Xiaopeng Tong (Tong et al. 2014). The figures were made using Generic Mapping Tools software (Wessel et al. 2013). This research was supported by the National Science Foundation (OCE-1128801, OCE-1536386), the Office of Naval Research (N000141712866), the Japan Science and Technology Agency (SATREPS 15543611), and the Japan Society for the Promotion of Science (KAKENHI 26000002).

This is a pre-copyedited, author-produced PDF of an article accepted for publication in *Geophysical Journal International* following peer review.

REFERENCES

Bassett, D. & Watts, A. B., 2015a. Gravity anomalies, crustal structure, and seismicity at subduction zones: 1. Seafloor roughness and subducting relief, *Geochemistry, Geophysics, Geosystems*, **16**(5), 1508–1540.

Bassett, D. & Watts, A. B., 2015b. Gravity anomalies, crustal structure, and seismicity at subduction zones: 2. Interrelationships between fore-arc structure and seismogenic behavior, *Geochemistry, Geophysics, Geosystems*, **16**(5), 1541–1576.

Billen, M., Cowgill, E., & Buer, E., 2007. Determination of fault friction from reactivation of abyssal-hill faults in subduction zones, *Geology*, **35**(9), 819–822.

Boston, B., Moore, G. F., Nakamura, Y., & Kodaira, S., 2014. Outer-rise normal fault development and influence on near-trench décollement propagation along the Japan Trench, off Tohoku, *Earth, Planets and Space*, **66**(1), 135.

Bry, M. & White, N., 2007. Reappraising elastic thickness variation at oceanic trenches, *Journal of Geophysical Research*, **112**(B8).

Burov, E. B. & Diament, M., 1995. The effective elastic thickness (T_e) of continental lithosphere: What does it really mean?, *Journal of Geophysical Research: Solid Earth*, **100**(B3), 3905–3927.

Byerlee, J., 1978. Friction of rocks, *Pure and applied geophysics*, **116**(4-5), 615–626.

Caldwell, J. G., Haxby, W. F., Karig, D. E., & Turcotte, D. L., 1976. On the applicability of a universal elastic trench profile, *Earth and Planetary Science Letters*, **31**(2), 239–246.

Cloetingh, S. & Burov, E. B., 1996. Thermomechanical structure of European continental lithosphere; constraints from rheological profiles and EET estimates, *Geophysical Journal International*, **124**(3), 695–723.

Coffin, M. F., Duncan, R. A., Eldholm, O., Fitton, J. G., Frey, F. A., Larsen, H. C., Mahoney, J. J., Saunders, A. D., Schlich, R., & Wallace, P. J., 2006. Large igneous provinces and scientific ocean drilling: Status quo and a look ahead, *Oceanography*, **19**(4), 150–160.

Contreras-Reyes, E. & Osses, A., 2010. Lithospheric flexure modelling seaward of the Chile trench: implications for oceanic plate weakening in the Trench Outer Rise region, *Geophysical Journal International*, **182**(1), 97–112.

Craig, T. J. & Copley, A., 2014. An explanation for the age independence of oceanic elastic thickness estimates from flexural profiles at subduction zones, and implications for continental rheology, *Earth and Planetary Science Letters*, **392**, 207–216.

Craig, T. J., Copley, A., & Jackson, J., 2014a. A reassessment of outer-rise seismicity and its implications for the mechanics of oceanic lithosphere, *Geophysical Journal International*, **197**(1), 63–89.

Craig, T. J., Copley, A., & Middleton, T. A., 2014b. Constraining fault friction in oceanic lithosphere using the dip angles of newly-formed faults at outer rises, *Earth and Planetary Science Letters*, **392**, 94–99.

Crosby, A. & McKenzie, D., 2009. An analysis of young ocean depth, gravity and global residual topography, *Geophysical Journal International*, **178**(3), 1198–1219.

Divins, D., 2003. Total sediment thickness of the world's oceans & marginal seas, NOAA National Geophysical Data Center, Boulder, CO.

Emry, E. L. & Wiens, D. A., 2015. Incoming plate faulting in the Northern and Western Pacific and implications for subduction zone water budgets, *Earth and Planetary Science Letters*, **414**, 176–186.

Emry, E. L., Wiens, D. A., & Garcia-Castellanos, D., 2014. Faulting within the Pacific plate at the Mariana Trench: Implications for plate interface coupling and subduction of hydrous minerals: Faulting at the Mariana Trench, *Journal of Geophysical Research: Solid Earth*, pp. n/a–n/a.

Faccenda, M., Gerya, T. V., & Burlini, L., 2009. Deep slab hydration induced by bending-related variations in tectonic pressure, *Nature Geoscience*, **2**(11), 790–793.

Fan, W., Shearer, P. M., Ji, C., & Bassett, D., 2016. Multiple branching rupture of the 2009 Tonga-Samoa earthquake, *Journal of Geophysical Research: Solid Earth*, **121**(8), 5809–5827.

Fujie, G., Kodaira, S., Kaiho, Y., Yamamoto, Y., Takahashi, T., Miura, S., & Yamada, T., 2018. Controlling factor of incoming plate hydration at the north-western Pacific margin, *Nature Communications*, **9**(1), 3844.

Garcia, E. S., Sandwell, D. T., & Luttrell, K. M., 2015. An iterative spectral solution method for thin elastic plate flexure with variable rigidity, *Geophysical Journal International*, **200**(2), 1010–1026.

Goetze, C. & Evans, B., 1979. Stress and temperature in the bending lithosphere as constrained by experimental rock mechanics, *Geophysical Journal International*, **59**(3), 463–478.

Hanks, T. C., 1971. The Kuril Trench-Hokkaido Rise System: Large Shallow Earthquakes and Simple Models of Deformation, *Geophysical Journal of the Royal Astronomical Society*, **23**(2), 173–189.

Hasterok, D., Chapman, D. S., & Davis, E., 2011. Oceanic heat flow: Implications for global heat loss, *Earth and Planetary Science Letters*, **311**(3), 386–395.

Hillier, J. K. & Watts, A., 2005. Relationship between depth and age in the North Pacific Ocean, *Journal of Geophysical Research: Solid Earth*, **110**(B2).

Hunter, J. & Watts, A., 2016. Gravity anomalies, flexure and mantle rheology seaward of circum-Pacific trenches, *Geophysical Journal International*, **207**(1), 288–316.

Kim, S.-S. & Wessel, P., 2011. New global seamount census from altimetry-derived gravity data, *Geophysical Journal International*, **186**(2), 615–631.

Kobayashi, K., Nakanishi, M., Tamaki, K., & Ogawa, Y., 1998. Outer slope faulting associated with the western Kuril and Japan trenches, *Geophysical Journal International*, **134**(2), 356–372.

Levitt, D. A. & Sandwell, D. T., 1995. Lithospheric bending at subduction zones based on depth soundings and satellite gravity, *Journal of Geophysical Research*, **100**(B1), 379.

Luttrell, K. & Sandwell, D., 2012. Constraints on 3-d stress in the crust from support of mid-ocean ridge topography, *Journal of Geophysical Research*, **117**(B4).

Manriquez, P., Contreras-Reyes, E., & Osses, A., 2014. Lithospheric 3-D flexure modelling of the oceanic plate seaward of the trench using variable elastic thickness, *Geophysical Journal International*, **196**(2), 681–693.

Massell, C. G., 2002. *Large-scale structural variation of trench outer slopes and rises*, Ph.D. thesis, University of California, San Diego.

Matthews, K. J., Müller, R. D., Wessel, P., & Whittaker, J. M., 2011. The tectonic fabric of the ocean basins, *Journal of Geophysical Research: Solid Earth*, **116**(B12).

McKenzie, D., Jackson, J., & Priestley, K., 2005. Thermal structure of oceanic and continental lithosphere, *Earth and Planetary Science Letters*, **233**(3), 337–349.

McNutt, M. K. & Menard, H. W., 1982. Constraints on yield strength in the oceanic lithosphere derived from observations of flexure, *Geophysical Journal International*, **71**(2), 363–394.

Mofjeld, H. O., Symons, C. M., Lonsdale, P., González, F. I., & Titov, V. V., 2004. Tsunami Scattering and Earthquake Faults in the Deep Pacific Ocean, *Oceanography*, **17**(1), 38–46.

Mueller, S. & Phillips, R. J., 1995. On the reliability of lithospheric constraints derived from models of outer-rise flexure, *Geophysical Journal International*, **123**(3), 887–902.

Mueller, S., Choy, G. L., & Spence, W., 1996. Inelastic models of lithospheric stress-I. Theory and application to outer-rise plate deformation, *Geophysical Journal International*, **125**(1), 39–53.

Müller, R. D., Sdrolias, M., Gaina, C., & Roest, W. R., 2008. Age, spreading rates, and spreading asymmetry of the world's ocean crust, *Geochemistry, Geophysics, Geosystems*, **9**(4).

Müller, R. D., Seton, M., Zahirovic, S., Williams, S. E., Matthews, K. J., Wright, N. M., Shephard, G. E.,

Maloney, K. T., Barnett-Moore, N., Hosseinpour, M., et al., 2016. Ocean Basin evolution and Global-Scale Plate Reorganization Events since Pangea Breakup, *Annual Review of Earth and Planetary Sciences*, **44**, 107–138.

Naif, S., Key, K., Constable, S., & Evans, R. L., 2015. Water-rich bending faults at the Middle America Trench, *Geochemistry, Geophysics, Geosystems*, **16**(8), 2582–2597.

Nakanishi, M., 2011. Bending-Related Topographic Structures of the Subducting plate in the Northwestern Pacific Ocean, in *Accretionary Prisms and Convergent Margin Tectonics in the Northwest Pacific Basin*, pp. 1–38, Springer.

Naliboff, J. B., Billen, M. I., Gerya, T., & Saunders, J., 2013. Dynamics of outer-rise faulting in oceanic-continental subduction systems, *Geochemistry, Geophysics, Geosystems*, **14**(7), 2310–2327.

Olson, C., Becker, J., & Sandwell, D., 2014. A new global bathymetry map at 15 arcsecond resolution for resolving seafloor fabric: SRTM15_PLUS, in *AGU Fall Meeting Abstracts*, vol. 1, p. 03.

Parsons, B. & Molnar, P., 1976. The Origin of Outer Topographic Rises Associated with Trenches, *Geophysical Journal International*, **1**(4), 707–712.

Parsons, B. & Sclater, J. G., 1977. An analysis of the variation of ocean floor bathymetry and heat flow with age, *Journal of Geophysical Research*, **82**(5), 803–827.

Ranero, C. R., Phipps Morgan, J., McIntosh, K., & Reichert, C., 2003. Bending-related faulting and mantle serpentinization at the Middle America trench, *Nature*, **425**(6956), 367–373.

Ritzwoller, M. H., Shapiro, N. M., & Zhong, S.-J., 2004. Cooling history of the Pacific lithosphere, *Earth and Planetary Science Letters*, **226**(1), 69–84.

Sandwell, D. T., Müller, R. D., Smith, W. H., Garcia, E., & Francis, R., 2014. New global marine gravity model from CryoSat-2 and Jason-1 reveals buried tectonic structure, *Science*, **346**(6205), 65–67.

Shillington, D. J., Bécel, A., Nedimović, M. R., Kuehn, H., Webb, S. C., Abers, G. A., Keranen, K. M., Li, J., Delescluse, M., & Mattei-Salicrup, G. A., 2015. Link between plate fabric, hydration and subduction zone seismicity in Alaska, *Nature Geoscience*, **8**(12), 961.

Tong, X., Smith-Konter, B., & Sandwell, D. T., 2014. Is there a discrepancy between geological and geodetic slip rates along the San Andreas Fault System?, *Journal of Geophysical Research: Solid Earth*, **119**(3), 2518–2538.

Turcotte, D. L. & Schubert, G., 2014. *Geodynamics*, Cambridge University Press, Cambridge, United Kingdom, 3rd edn.

Van Avendonk, H. J., Holbrook, W. S., Lizarralde, D., & Denyer, P., 2011. Structure and serpentinization of the subducting Cocos plate offshore Nicaragua and Costa Rica, *Geochemistry, Geophysics, Geosystems*, **12**(6).

Ventsel, E. & Krauthammer, T., 2001. *Thin Plates and Shells: Theory: Analysis, and Applications*, CRC Press, New York, NY, USA, 680 pp.

Walcott, R., 1970. Flexural Rigidity, Thickness, and Viscosity of the Lithosphere, *Journal of Geophysical Research*, **75**(20), 3941–3954.

Watts, A. & Talwani, M., 1974. Gravity Anomalies Seaward of Deep-Sea Trenches and their Tectonic Impli-

cations, *Geophysical Journal International*, **36**(1), 57–90.

Watts, A. B., 2001. *Isostasy and Flexure of the Lithosphere*, Cambridge University Press, Cambridge ; New York.

Wessel, P., 1992. Thermal Stresses and the Bimodal Distribution of Elastic Thickness Estimates of the Oceanic Lithosphere, *Journal of Geophysical Research: Solid Earth*, **97**(B10), 14177–14193.

Wessel, P., 1996. Analytical solutions for 3-D flexural deformation of semi-infinite elastic plates, *Geophysical Journal International*, **124**(3), 907–918.

Wessel, P., Smith, W. H., Scharroo, R., Luis, J., & Wobbe, F., 2013. Generic mapping tools: improved version released, *Eos, Transactions American Geophysical Union*, **94**(45), 409–410.

Wessel, P., Matthews, K. J., Müller, R. D., Mazzoni, A., Whittaker, J. M., Myhill, R., & Chandler, M. T., 2015. Semiautomatic fracture zone tracking, *Geochemistry, Geophysics, Geosystems*, **16**(7), 2462–2472.

Whittaker, J. M., Goncharov, A., Williams, S. E., Müller, R. D., & Leitchenkov, G., 2013. Global sediment thickness data set updated for the Australian-Antarctic Southern Ocean, *Geochemistry, Geophysics, Geosystems*, **14**(8), 3297–3305.

Zhang, F., Lin, J., & Zhan, W., 2014. Variations in oceanic plate bending along the Mariana trench, *Earth and Planetary Science Letters*, **401**, 206–214.

Zhang, F., Lin, J., Zhou, Z., Yang, H., & Zhan, W., 2017. Intra-and intertrench variations in flexural bending of the Manila, Mariana and global trenches: implications on plate weakening in controlling trench dynamics, *Geophysical Journal International*, **212**(2), 1429–1449.

Zhang, J., Sun, Z., Xu, M., Yang, H., Zhang, Y., & Li, F., 2018. Lithospheric 3-d flexural modelling of subducted oceanic plate with variable effective elastic thickness along the Manila Trench, *Geophysical Journal International*.

Zhong, S. & Watts, A., 2013. Lithospheric deformation induced by loading of the Hawaiian Islands and its implications for mantle rheology, *Journal of Geophysical Research: Solid Earth*, **118**(11), 6025–6048.

Zhou, Z. & Lin, J., 2018. Elasto-plastic deformation and plate weakening due to normal faulting in the subducting plate along the Mariana Trench, *Tectonophysics*, **734**, 59–68.

Zhou, Z., Lin, J., Behn, M. D., & Olive, J.-A., 2015. Mechanism for normal faulting in the subducting plate at the Mariana Trench, *Geophysical Research Letters*, **42**(11), 4309–4317.